JGR Space Physics

RESEARCH ARTICLE
10.1029/2026JA035261

Modeling the Detectability of Energetic Heliospheric Ions at Pluto During the New Horizons Flyby

Randall T. Ruch[1], **Sven Simon**[1,2], **Peter Kollmann**[3], **and C. Michael Haynes**[1]

[1]School of Earth and Atmospheric Sciences, Georgia Institute of Technology, Atlanta, GA, USA, [2]School of Physics, Georgia Institute of Technology, Atlanta, GA, USA, [3]The Johns Hopkins University Applied Physics Laboratory, Laurel, MD, USA

Key Points:

- We model the detectability of energetic heliospheric helium ions by Pluto Energetic Particle Spectrometer Science Investigation (PEPSSI) during New Horizons' flyby through Pluto's induced magnetosphere
- The observability of substantial reductions in helium ion flux within the interaction region strongly depends on PEPSSI's viewing geometry
- The perturbations to the modeled helium ion fluxes into the PEPSSI detector gradually decrease with energy, in contrast to the observed ones

Correspondence to:
R. T. Ruch,
randy.ruch@eas.gatech.edu

Citation:
Ruch, R. T., Simon, S., Kollmann, P., & Haynes, C. M. (2026). Modeling the detectability of energetic heliospheric ions at Pluto during the new horizons flyby. *Journal of Geophysical Research: Space Physics*, *131*, e2026JA035261. https://doi.org/10.1029/2026JA035261

Received 20 FEB 2026
Accepted 15 APR 2026

Abstract We investigate the detectability of heliospheric helium ions at energies up to 100 keV by the New Horizons (NH) spacecraft during its flyby through Pluto's induced magnetosphere. The Pluto Energetic Particle Spectrometer Science Investigation energetic ion detector observed a reduction in their flux by an order of magnitude as the spacecraft passed through the non-uniform electromagnetic fields near the dwarf planet. This is despite these ions gyrating on scales up to several hundred Pluto radii. To contextualize these observations, we incorporate the electromagnetic fields from a hybrid model into a novel tracing tool for energetic He^+ and generate synthetic time series of their flux into the detector along the NH trajectory and several hypothetical, idealized flyby geometries. Our major results are: (a) The detectability of perturbations to He^+ fluxes highly depends on PEPSSI's look direction. Even along the same flyby trajectory, different viewing geometries may reveal changes in helium flux by up to a factor of five or no perturbations whatsoever. (b) The substantial reductions in He^+ flux seen by NH may largely stem from the detector's finite field-of-view, filtering the incoming particles in velocity space. Without this effect, the reduction in flux by the draped fields would not exceed a factor of two. (c) The modeled flux perturbations gradually decrease with energy and become indiscernible above 20 keV. This behavior is qualitatively consistent with energetic ion dynamics at other small solar system bodies. (d) Across the range of plausible interplanetary field orientations, the model persistently suggests weaker reductions in He^+ flux than observed.

1. Introduction

Pluto (radius $R_P = 1,188$ km) is a dwarf planet orbiting the Sun at distances between 30 and 50 AU. The Pluto system was visited for the first and only time during the flyby of the NH spacecraft on 14 July 2015, as the dwarf planet was at a heliocentric distance near 33 AU. Observations from this event revealed that molecular nitrogen (N_2) is the primary constituent of Pluto's atmosphere at altitudes below 1,400 km, above which methane (CH_4) begins to dominate (Gladstone et al., 2016; Young et al., 2017). The ionization of N_2 and CH_4 via charge exchange with solar wind ions and photoionization by solar UV photons leads to the formation of the dwarf planet's ionosphere (Hinson et al., 2018; Krasnopolsky, 2020). Freshly generated N_2^+ and CH_4^+ ions are picked up by the electromagnetic fields of the solar wind. Mass loading by this population of heavy Plutogenic ions slows the supermagnetosonic solar wind (magnetosonic Mach number $M_{MS} \approx 10$), generating a bow shock 4–5 R_P upstream of Pluto's center (Bagenal et al., 2016; McComas et al., 2016). This interaction between the dwarf planet's atmosphere and the solar wind also perturbs the interplanetary magnetic field (IMF), leading to, for example, the formation of a magnetic pileup region at Pluto's ramside and a magnetotail that extends toward downstream (e.g., Feyerabend et al., 2017). The interaction region, encompassing the tail of Plutogenic pickup ions and the perturbations of the IMF, constitutes the dwarf planet's *induced magnetosphere*.

Being so far out in the heliosphere, the strength of the IMF at Pluto (~0.1 nT) is more than an order of magnitude lower than at Earth (Bagenal et al., 2015). Therefore, the Plutogenic N_2^+ and CH_4^+ pickup ions possess gyroradii between 10^2 and 10^3 R_P. Additionally, the radial component of the IMF decreases with distance from the Sun faster than its azimuthal component; this leads the IMF at Pluto to be largely aligned (or anti-aligned) with the dwarf planet's orbital motion. As a result, the pickup ions begin their initial gyromotion by moving along the direction of the convective electric field with near-ballistic trajectories, either northward or southward of Pluto's orbital plane depending on the direction of the IMF. To conserve the total momentum of the plasma, the solar wind is diverted in the opposite direction, causing Pluto's induced magnetosphere to be highly asymmetric across its orbital plane (e.g., Barnes et al., 2019; Delamere, 2009; Feyerabend et al., 2017). In addition to the pickup tail

formed by the cycloidal motion of the heavy ions, the dwarf planet's plasma wake also contains a dense, narrow region of Plutogenic ions extending toward downstream along the Sun-Pluto line (Feyerabend et al., 2017; McComas et al., 2016). Analogous to the magnetopause at Earth, a "Plutopause" is formed that largely excludes the solar wind from the heavy ion tail (McComas et al., 2016). The deflected solar wind stretches the magnetic pileup region toward downstream, leading to an enhancement in field strength along the Plutopause (e.g., Feyerabend et al., 2017; Ruch et al., 2025).

The NH spacecraft did not carry a magnetometer, so the IMF at the time of the flyby could not be measured directly. Nonetheless, magnetic field data collected by Voyager 2 from 25 to 39 AU have been used to constrain the strength of the IMF during the NH flyby between 0.08 and 0.30 nT (Bagenal et al., 2015). The Solar Wind Around Pluto (SWAP) instrument aboard NH measures the energy-per-charge ratio (E/q) of ions from about 35 eV/q to more than 7.5 keV/q (McComas et al., 2007). Just a few minutes after NH's closest approach to Pluto, as the spacecraft was a distance of about 12 R_P from the dwarf planet's center and 7 R_P downstream, SWAP detected an influx of low-energy ($\lesssim$1 keV/q) Plutogenic pickup ions at the start of their cycloidal motion (McComas et al., 2016). Zirnstein et al. (2016) modeled the trajectories of these ions for various IMF orientations, concluding that an IMF component antiparallel to the direction of Pluto's orbital motion is required to explain SWAP observations. Hybrid simulations (kinetic ions, fluid electrons) of Pluto's interaction with the solar wind have been carried out by Barnes et al. (2019) and Feyerabend et al. (2017) to further constrain the strength and orientation of the IMF during the NH flyby. These studies found field magnitudes most suitable to explain the observed deceleration pattern of the solar wind to be 0.1 and 0.24 nT, respectively. Using the IMF orientation determined by Zirnstein et al. (2016), their models were able to reproduce the velocity profile of the solar wind observed by SWAP as NH crossed Pluto's bow shock.

In addition to the thermal ions from the solar wind and the Plutogenic pickup ions, the dwarf planet is embedded in a population of *energetic heliospheric ions* (H^+, He^+) with energies from a few keV up to several MeV (Kollmann, Hill, Allen, et al., 2019). This energetic component consists of interstellar pickup ions and suprathermal ions. The former population is generated through ionization of neutral interstellar gas in the outer heliosphere, for example, via charge exchange or photoionization (Fisk & Gloeckler, 2007). These freshly generated ions are accelerated by the convective electric field of the solar wind, causing them to gyrate and drift at the solar wind bulk velocity $\vec{u}_{\rm SW}$. Hence, the interstellar pickup ions can reach a maximum energy of $E_c = \frac{1}{2} m|2\vec{u}_{\rm SW}|^2$, where m is the ion mass. This corresponds to the peak velocity of $2\vec{u}_{\rm SW}$ reached by these ions when the velocity vector of their gyration conspires in the same direction as their drift. The suprathermal population is constituted by interstellar pickup ions that have undergone acceleration to energies above E_c (Fisk & Gloeckler, 2007). The additional speedup may be caused by, for example, diffusive shock acceleration (Bell, 1978), or the transfer of energy by repeated adiabatic compression and expansion of the solar wind downstream of an interplanetary shock (Fisk & Gloeckler, 2014).

During the flyby, the PEPSSI instrument aboard NH measured the differential intensity of energetic heliospheric He^+ ions from about 2 keV to near 100 keV (Kollmann, Hill, Allen, et al., 2019). The corresponding gyroradii of these ions range between a few dozen and several hundred R_P. When NH was about 13 R_P away from Pluto's center and 8 R_P downstream, the observed flux of energetic He^+ ions displayed an abrupt increase, which was interpreted as a large fraction of this population being deflected by the perturbed fields toward the instrument's field-of-view (FOV; Bagenal et al., 2016). A few minutes later as NH was about 20 R_P downstream of Pluto, PEPSSI observed an order of magnitude decrease in He^+ differential intensity, compared to the level measured upstream in the unperturbed solar wind (Kollmann, Hill, Allen, et al., 2019). In Pluto's wake, the flux of energetic He^+ ions seen by PEPSSI was decreased in this way across the entire energy range sampled. This depletion immediately began replenishing exponentially with distance along the Sun-Pluto line, gradually returning to the unperturbed level over about 190 R_P downstream (Kollmann, Hill, Allen, et al., 2019).

Ruch et al. (2025) developed a model to investigate the deflection pattern of energetic He^+ ions as they interact with Pluto's induced magnetosphere. These authors employed a particle tracing tool to propagate the heliospheric ions through the perturbed fields of the induced magnetosphere, as calculated by the AIKEF hybrid model (Müller et al., 2011). Their approach determined the flux of energetic He^+ ions through a hypothetical, infinitely extended, plane detector downstream of Pluto, oriented perpendicular to the Sun-Pluto line. For an IMF anti-parallel to the direction of the dwarf planet's orbital motion, the model of Ruch et al. (2025) revealed that the deflection of energetic He^+ by the perturbed fields generates a region of depleted flux mainly north of Pluto's

orbital plane, and a corresponding enhancement to its south. If the IMF is oriented oppositely, the locations of the modeled perturbations in He^+ flux are mirrored across the plane. These non-uniformities in flux through the detector plane arise as the energetic ions are deflected when they travel through, for example, the stretched magnetic pileup region where the field strength is enhanced relative to the IMF (Ruch et al., 2025). The elevated field strength locally causes the ions' gyroradii to decrease; for an IMF antiparallel to Pluto's orbital motion, this bends their trajectories southward.

Ruch et al. (2025) also found the deflection of He^+ in Pluto's induced magnetosphere to be energy-dependent: in the low keV regime, the ions are more heavily deflected, whereas above 100 keV, they travel through the interaction region without significant changes to their trajectories. This pattern maps into the modeled particle fluxes: for 2 keV He^+ ions, the plane detector sees changes in flux by nearly a factor of two, whereas at 100 keV, it only observes perturbations below 9%. Such a dependence on energy is consistent with energetic ion behavior in the perturbed electromagnetic fields near, for example, Callisto (Liuzzo et al., 2019a) and Europa (Addison et al., 2021; Haynes et al., 2023; Nordheim et al., 2022). The modeled regions of perturbed flux extend about 200 R_P downstream of Pluto, consistent with estimates from PEPSSI observations (Kollmann, Hill, Allen, et al., 2019).

The energy dependence of the inhomogeneities in He^+ flux found by Ruch et al. (2025) contrasts the NH observations which revealed a persistent depletion in downstream fluxes across all energies observed. Further, the greatest reduction in He^+ flux through their model detector is by less than a factor of two, whereas PEPSSI observed the fluxes between 2 and 100 keV to drop by an entire order of magnitude. A similar behavior was suggested in the PhD thesis of Barnes (2024): this modeling study revealed that, in order to generate significant reductions in energetic He^+ flux, the IMF near Pluto must be above the range proposed by Bagenal et al. (2015).

The discrepancies between the model results of Ruch et al. (2025) and observations may partially stem from differences in detector geometry. The PEPSSI instrument can be considered point-like on the length scales of Pluto's interaction region, so the number of ions that reach the instrument is orders of magnitude smaller than the number intercepting the plane detector of Ruch et al. (2025). Of the ions reaching PEPSSI, only those with a velocity that allows them to enter the instrument's $160° \times 12°$ FOV can be captured (McNutt et al., 2008). In contrast, the planar detector of Ruch et al. (2025) accepts all impinging ions regardless of their velocity vector. Due to He^+ gyroradii in excess of dozens of R_P, the southward deflection of these ions in the induced magnetosphere could render some of them undetectable, for example, by an instrument whose boresight vector has a southward component. Such a detector orientation occurred when PEPSSI identified the depletion in He^+ flux (see also Kollmann, Hill, Allen, et al., 2019). Thus, it is possible that NH only captured a part of the deflected He^+ population in which the flux depletion seen by the instrument was particularly strong. Therefore, the goal of our study is to determine how the PEPSSI instrument's position and the orientation of its FOV could have affected the energetic ion observations during the NH flyby.

For this purpose, we have developed a novel tracing model to propagate energetic He^+ ions through Pluto's induced magnetosphere and calculate their flux into a synthetic PEPSSI detector along the NH trajectory. This will be done for a detector with a time-dependent look direction, identical to that of PEPSSI during the flyby. To further constrain the influence of the viewing geometry on the detectability of deflected He^+ ions, we will also consider several cases in which the detector has fixed, idealized look directions. Analogous to the approach of Ruch et al. (2025), we employ the 3D output of the AIKEF hybrid model to describe the non-uniform fields encountered by the ions in Pluto's induced magnetosphere within our particle tracer.

This paper is structured as follows: the setup of the hybrid model and a detailed description of our particle tracing tool are outlined in Section 2. The results of our model calculations and their implications for the interpretation of PEPSSI observations are discussed in Section 3. A summary of our major findings is given in Section 4.

2. Modeling Energetic Ion Dynamics Near Pluto

Multiple Cartesian frames of reference are used in our model. The first is the Pluto-centered frame, Σ_P, which is at rest with respect to the dwarf planet's position. This frame is used in AIKEF to model the electromagnetic field perturbations from Pluto's interaction with the solar wind. The second is the rest frame of the NH spacecraft, Σ_{NH}, which moves at an approximately constant velocity $\vec{u}_{NH}$ with respect to Σ_P and is centered on the spacecraft. This is the frame in which the PEPSSI instrument measured the energies of incident He^+ ions. The third is the rest

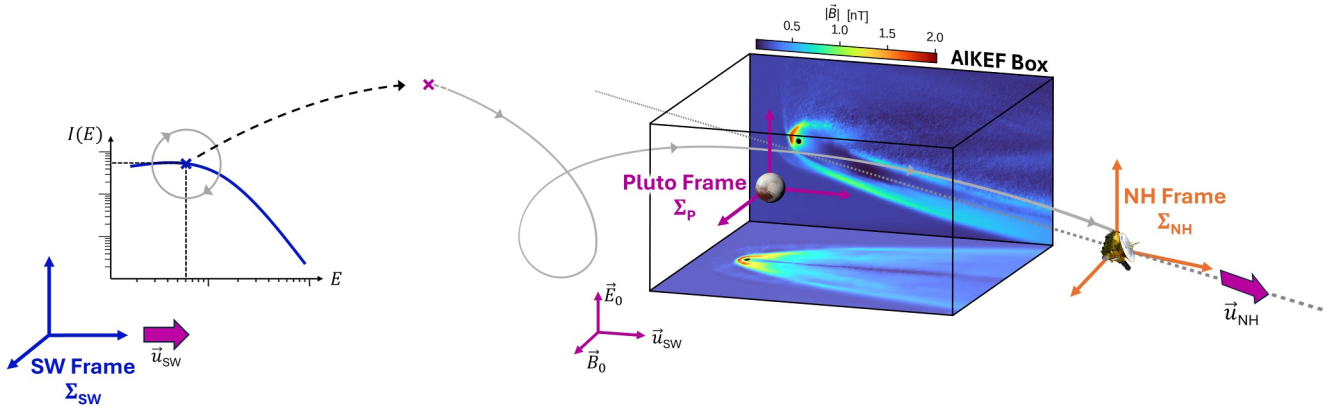

Figure 1. Illustration of the process for determining the flux of an ion macroparticle into the Pluto Energetic Particle Spectrometer Science Investigation (PEPSSI) detector. The frames of reference used in this study (Σ_{SW}, Σ_P, Σ_{NH}) are represented by uniquely colored axes. The magenta vectors next to the Σ_{SW} and Σ_{NH} frames indicate their motion relative to the Σ_P frame. Pluto and the New Horizons spacecraft are depicted at the center of their respective frames. The black cuboid represents the domain of the AIKEF hybrid model, with two colormaps of the magnetic field strength from Ruch et al. (2025) on its "walls." A sample He^+ trajectory is shown (light gray), entering the PEPSSI instrument along the spacecraft's flyby path (dotted, dark gray). The arrows along the ion's trajectory indicate the direction of its motion as it travels from upstream toward the instrument. In our model, ions are launched at the position of PEPSSI and then traced backward in time until they reach the "escape plane" at $x = -762\ R_P$, indicated by the magenta cross. The particle's velocity at that location is recorded. The corresponding energy (blue cross) is used to sample the $I(E)$ spectrum observed by PEPSSI upstream of Pluto (blue curve). The circular trajectory overlain on the energy spectrum (light gray) exemplifies the shape of an He^+ trajectory in a plane perpendicular to the magnetic field in the solar wind frame Σ_{SW} where its drift motion disappears.

frame of the unperturbed solar wind, Σ_{SW}, which moves at constant velocity $\vec{u}_{SW}$ (along the Sun-Pluto line) relative to Σ_P.

The x-axis of the Pluto frame Σ_P is directed from the Sun to the dwarf planet. The y-axis is defined by the component of Pluto's orbital motion perpendicular to the x-axis, pointing in the prograde direction. Thus, the x and y-axes span Pluto's orbital plane. The z-axis completes the right-handed system, pointing northward. The corresponding set of orthonormal basis vectors is denoted by $\{\vec{e}_x, \vec{e}_y, \vec{e}_z\}$. The coordinate axes of the spacecraft frame Σ_{NH} and the solar wind frame Σ_{SW} are each parallel to these vectors $\{\vec{e}_x, \vec{e}_y, \vec{e}_z\}$. Another Cartesian coordinate system (x', y', z') is introduced later in Section 2.2 to describe the FOV of our model detector; its axes are generally not aligned with the basis vectors $\{\vec{e}_x, \vec{e}_y, \vec{e}_z\}$.

Figure 1 illustrates the overall setup of our particle tracing model. We launch energetic He^+ ions from the instantaneous position of the PEPSSI detector at many equidistant points along the spacecraft trajectory (dotted, dark gray). The energies of these ions are in the range measured by PEPSSI during the Pluto flyby. These ions are then traced *backward in time* (i.e., with a negative timestep $\Delta t < 0$) from the detector through the dwarf planet's induced magnetosphere, until they reach the region far upstream of Pluto where the fields are unperturbed (magenta cross). The energy spectrum $I(E)$ measured by PEPSSI upstream of the dwarf planet (blue curve) is sampled at the ion's energy in the upstream region. The ion flux into the detector can then be determined with Liouville's theorem (analogous to Ruch et al., 2025). By totaling the contributions from ions at a given energy, we then construct time series of the He^+ flux captured by our synthetic PEPSSI detector. In the following subsections, we provide details on the various components of our model: the treatment of the electromagnetic fields (Section 2.1), the emulation of the PEPSSI detector and the launching of energetic ions (Section 2.2), the approach for tracing the ions backward in time (Section 2.3), the determination of the ion flux into the detector (Section 2.4 and Appendix A), and the spacecraft trajectories and detector viewing geometries considered (Section 2.5). For reference, an overview of the nomenclature used throughout this section is provided in Table 1.

2.1. Pluto's Electromagnetic Environment

We adopt the existing output of the AIKEF hybrid model from the study of Ruch et al. (2025) to describe the electromagnetic fields in the vicinity of the dwarf planet. In addition to Pluto (e.g., Feyerabend et al., 2017), the AIKEF model has an extensive history of application to other small bodies in the solar system, such as Titan (e.g., Simon et al., 2006; Tippens et al., 2022; Tippens, Roussos, et al., 2024; Tippens, Simon, & Roussos, 2024), Europa (e.g., Addison et al., 2021; Addison et al., 2022, 2023, 2024; Haynes et al., 2023; Haynes, Tippens,

Table 1
Overview of the Various Subscripts and Indices Used Throughout Section 2

Script	Definition
f	"final" quantity for a macroparticle when captured by the detector, at the *start* of the backtracing procedure
i	"initial" quantity for a macroparticle as it reaches the "escape plane", at the *end* of the backtracing procedure
P	quantity in the Pluto rest frame Σ_{P}
NH	quantity in the spacecraft rest frame Σ_{NH}
SW	quantity in the rest frame of the unperturbed solar wind Σ_{SW}
$\lambda \in [1, N]$	index for one of N macroparticles backtraced from node $\vec{r}_f$ (along the NH trajectory) with a given energy $E_{f,\mathrm{NH}}$

et al., 2025), Callisto (e.g., Liuzzo et al., 2015; Liuzzo et al., 2016, 2017, 2024), and Ganymede (e.g., Haynes, Simon, & Liuzzo, 2025; Stahl et al., 2023). In the following, we provide a brief overview of the input parameters used for the AIKEF model run of Ruch et al. (2025). Detailed justifications for the chosen parameter set as well as visuals and an analysis of the output are provided in Sections 2.1 and 3.1 of their study.

The electromagnetic fields from AIKEF are calculated in the Σ_{P} frame. The thermal ions in the solar wind are represented with a population of protons, characterized by a drifting Maxwellian distribution with bulk velocity $\vec{u}_{\mathrm{SW}} = 403$ km/s $\vec{e}_x$, number density $n_0 = 0.025$ cm^{-3}, and temperature $kT = 0.66$ eV (see also Bagenal et al., 2016). The study of Feyerabend et al. (2017) showed that such a setup is capable of reproducing the observed deceleration profile of the solar wind across Pluto's bow shock. Therefore, instead of including the energetic heliospheric He^+ ions self-consistently within the hybrid model, we treat them as test particles with our backtracing tool (analogous to Ruch et al., 2025).

As discussed in detail by Ruch et al. (2025), the AIKEF model uses a background IMF of $\vec{B}_0 = -0.24$ nT $\vec{e}_y$; that is, it is antiparallel to Pluto's orbital motion (Zirnstein et al., 2016). The resulting convective electric field $\vec{E}_0 = -\vec{u}_{\mathrm{SW}} \times \vec{B}_0$ points northward along $+\vec{e}_z$. These input parameters yield a plasma beta of $\beta = 0.29$, Alfvén speed of $v_{\mathrm{A},0} = 33$ km/s, and magnetosonic Mach number of $M_{\mathrm{MS}} = 10.7$. Observations by SWAP and PEPSSI show nearly no difference between the unperturbed (thermal and energetic) solar wind parameters in the inbound (before 06:00 UTC) and outbound (after 20:00 UTC) legs of the encounter (Kollmann, Hill, Allen, et al., 2019; McComas et al., 2016). This suggests that the notion of an interaction with a steady-state upstream flow is suitable for the NH flyby. In the model, Pluto's atmosphere consists of N_2 and CH_4, with the altitude profiles for their number densities represented by a sum of barometric laws (analogous to Feyerabend et al., 2017). The dwarf planet's ionosphere is produced from the neutral gas through photoionization by solar UV photons and charge exchange with the upstream protons. Pluto is the only obstacle included in the AIKEF domain; that is, we do not take into account, for instance, the presence of Charon. During the NH flyby, this moon was devoid of a detectable atmosphere and ionosphere (Gladstone et al., 2016; Stern et al., 2017). Hence, we do not expect Charon to have a significant impact on the field perturbations and their role in the observability of possible energetic ion depletions by PEPSSI.

The cuboidal AIKEF domain extends from $x = -20\ R_P$ to $x = 100\ R_P$, and from $y, z = -32\ R_P$ to $y, z = 32\ R_P$ (black in Figure 1). Since He^+ gyroradii at the highest energies considered ($\sim 10^2\ R_P$) are comparable to the length of this domain, the fields from AIKEF cannot be used as the sole input for our particle tracer. Thus, outside its bounds, the fields acting upon the energetic He^+ ions are treated as *uniform* with values of $\vec{E}_0$ and $\vec{B}_0$ (analogous to Ruch et al., 2025). The large size of the AIKEF domain ensures that the electromagnetic fields return approximately to their ambient values at its outer faces. Hence, the trajectories of the He^+ ions do not experience any appreciable deflection when transitioning into the uniform fields outside (see also Ruch et al., 2025).

2.2. Modeling the PEPSSI Detector and Launching Energetic Ions

In order to emulate PEPSSI observations of energetic ions along a spacecraft trajectory, our particle tracing model must account for the instrument's finite FOV and infinitesimal size relative to, for example, the extension of

Pluto's induced magnetosphere or the ion gyroradii. If we traced the ions forward in time ($\Delta t > 0$), for example, by launching them at the nodes of a planar grid far upstream of Pluto (as done by Ruch et al., 2025), only a minuscule fraction of them would intercept the point-like detector at a given position with a velocity vector favorable for capture by its FOV. Thus, the model would spend a majority of its computation time calculating the trajectories of ions that do not even enter the detector.

Instead, we launch He^+ ion macroparticles—each representing a large number of real ions from a similar region of phase space—at the momentary position of the detector. These ions are then traced *backward* in time (timestep $\Delta t < 0$) as they travel through Pluto's induced magnetosphere toward upstream. This approach allows us to calculate only the trajectories of those ions that do enter the detector (see also Haynes, Simon, & Liuzzo, 2025; Haynes, Tippens, et al., 2025; Tippens, Roussos, et al., 2024; Tippens, Simon, & Roussos, 2024). The ion macroparticles start the backtracing process at PEPSSI's momentary location with the "*final*" position $\vec{r}_f$ and velocity $\vec{v}_f$ that they have as they are captured by the instrument.

The PEPSSI instrument accepts charged particles through a fan-like FOV of 160° azimuth by 12° elevation, defined by the instrument's internal geometry (McNutt et al., 2008). The FOV is subdivided into six sectors (S0, S1, …, S5), each covering a solid angle of 25° × 12°, leaving a 2° azimuthal separation between neighboring sectors. The depletion in energetic He^+ flux downstream of Pluto was identified in data from the S0 sector while its boresight $\vec{L}$ (at the center of its FOV) was tilted by 34° southward from the Sun-Pluto line (Bagenal et al., 2016; Kollmann, Hill, Allen, et al., 2019). Our analysis focuses on sector S0, so the FOV of the detector in our model is 25° × 12°.

A large number of He^+ macroparticles are launched from discrete, equidistant points ("nodes") at positions $\vec{r}_f$ along the spacecraft trajectory. At every node, each macroparticle is assigned a unique final velocity vector $\vec{v}_{f,\mathrm{NH}}$ that differs in magnitude and/or direction from those of other ion macroparticles launched at the same node. Here, the term "final" always refers to the instant of the ion's detection by the instrument. The vectors $\vec{v}_{f,\mathrm{NH}}$ are defined in Σ_{NH}, since this is the frame in which they are measured by PEPSSI. The magnitude of an ion's final velocity depends on the energy $E_{f,\mathrm{NH}}$ that it possesses (in the Σ_{NH} frame) when entering the detector: $|\vec{v}_{f,\mathrm{NH}}| = \sqrt{2E_{f,\mathrm{NH}}/m}$, where $m = 4$ amu is the mass of He^+. We consider 17 logarithmically spaced values for $E_{f,\mathrm{NH}}$ spanning the same energy range as the observed spectra of Kollmann, Hill, Allen, et al. (2019): $E_{f,\mathrm{NH}} \in \{2.3, 2.6, 3.6, 4.5, 5.7, 7.2, 9.0, 11.3, 14.2, 17.8, 22.4, 28.2, 35.4, 44.5, 55.9, 70.3, 88.3\}$ keV. Actual time-of-flight data from PEPSSI (below 100 keV) are binned into six channels, each spanning a certain energy range (McNutt et al., 2008). In order to emulate the time series observed by a certain channel, the fluxes at all energies $E_{f,\mathrm{NH}}$ within its range need to be taken into account. Our investigation will focus on channel L09 which covers the energy range from $E_{f,\mathrm{NH}} = 9.52$ keV to $E_{f,\mathrm{NH}} = 18.00$ keV: measurements from this channel were analyzed in detail by Kollmann, Hill, Allen, et al. (2019).

At any given node $\vec{r}_f$ along the spacecraft trajectory, the possible orientations of the He^+ ions' final velocity vectors $\vec{v}_{f,\mathrm{NH}}$ are determined by the FOV of our model detector. To describe them, a new Cartesian coordinate system (x', y', z') is introduced. This system is centered on the "apex" of the detector, that is, the focal point of S0. Its location approximately corresponds to the center of the instrument's time-of-flight chamber (McNutt et al., 2008). This system is at rest with respect to the Σ_{NH} frame, with its axes defined by the momentary orientation of the detector at trajectory node $\vec{r}_f$. Thus, at any given node, the magnitude of an ion's final velocity vector $\vec{v}_{f,\mathrm{NH}}$ is the same between Σ_{NH} and the (x', y', z') system. The orientation of the S0 sector's FOV within the "primed" coordinate system is illustrated in Figure 2. The x'-axis is aligned with the sector's boresight vector $\vec{L}$, pointing radially outward at the center of its FOV (green). The "equatorial" plane of sector S0 is spanned by the x' and y'-axes, with the z'-axis perpendicular to both. We introduce geographic coordinates (θ_v, ϕ_v), where latitude θ_v is measured against the detector's equatorial plane ($z' = 0$); the values of θ_v are positive for $z' > 0$ and negative for $z' < 0$. Longitude ϕ_v is measured within the detector's equatorial plane, against the positive x'-axis. The S0 sector's FOV possesses latitudinal and longitudinal extensions of $\Delta\theta_v = 12°$ and $\Delta\phi_v = 25°$, respectively, centered on the boresight $\vec{L}$. Individual look directions within the sector's FOV are given by unit vectors $\vec{l}(\theta_v, \phi_v)$, with the boresight $\vec{L} = \vec{l}(0°, 0°) = (1, 0, 0)$. An ion's final velocity vector $\vec{v}'_{f,\mathrm{NH}}$ in the (x', y', z') system can then be written as

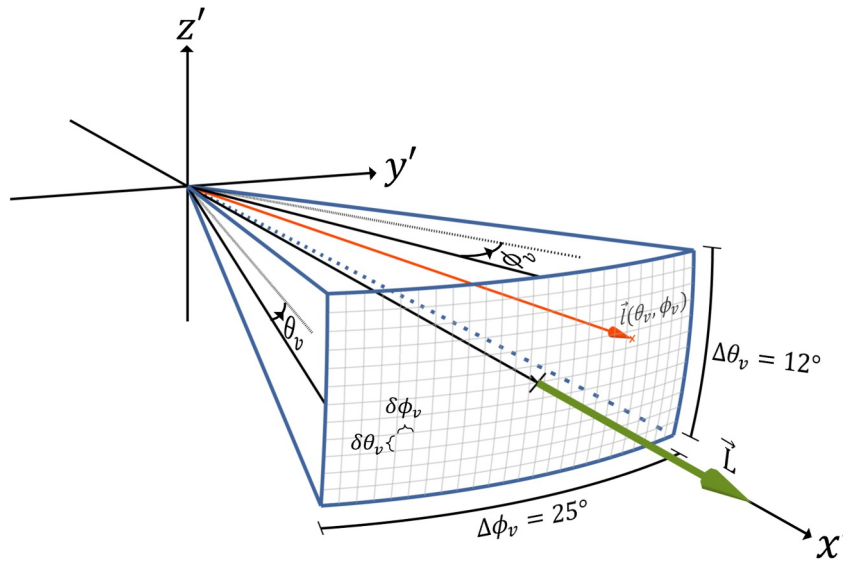

Figure 2. Cartesian coordinate system (x', y', z') to describe the FOV of PEPSSI's sector S0. The boresight vector $\vec{L}$ (green) at the center of the FOV is aligned with the x'-axis. The FOV (blue) is defined by a latitudinal extension of $\Delta\theta_v = 12°$ and a longitudinal extension of $\Delta\phi_v = 25°$. The arrowheads attached to the angles between the solid and dotted black lines on the top and left boundaries of the FOV show the direction of increase for ϕ_v and θ_v, respectively. The grid discretizing the FOV illustrates the angular separation between neighboring look directions $\vec{l}(\theta_v, \phi_v)$ by increments of $\delta\theta_v$ and $\delta\phi_v$. Vectors $\vec{l}(\theta_v, \phi_v)$ indicating a specific look direction within the FOV point from the origin to the center of each cell on the grid; a sample look direction, $\vec{l}(1.5°, 7.0°)$, is shown in orange.

$$\vec{v}'_{f,\mathrm{NH}} = -\vec{l}\sqrt{\frac{2E_{f,\mathrm{NH}}}{m}} = -\sqrt{\frac{2E_{f,\mathrm{NH}}}{m}}\begin{pmatrix}\cos\theta_v\cos\phi_v\\ \cos\theta_v\sin\phi_v\\ \sin\theta_v\end{pmatrix} \quad . \tag{1}$$

In our model, θ_v and ϕ_v are each discretized in increments of $\delta\theta_v = \delta\phi_v = 1°$, with $\theta_v \in \left[-\frac{\Delta\theta_v}{2} + \frac{\delta\theta_v}{2}, \frac{\Delta\theta_v}{2} - \frac{\delta\theta_v}{2}\right]$ and $\phi_v \in \left[-\frac{\Delta\phi_v}{2} + \frac{\delta\phi_v}{2}, \frac{\Delta\phi_v}{2} - \frac{\delta\phi_v}{2}\right]$. This is illustrated by the light gray grid across the FOV in Figure 2; look directions $\vec{l}(\theta_v, \phi_v)$ point through the center of the cells on this grid. This discretization results in $\frac{\Delta\theta_v}{\delta\theta_v} = 12$ points in latitude and $\frac{\Delta\phi_v}{\delta\phi_v} = 25$ points in longitude, or $N = \frac{\Delta\theta_v}{\delta\theta_v}\frac{\Delta\phi_v}{\delta\phi_v} = 300$ unique directions $\vec{l}$ from which ion macroparticles are launched at a given node $\vec{r}_f$ for each energy $E_{f,\mathrm{NH}}$. We note that increasing the value of N (i.e., further refining the FOV discretization) does not have any significant impact on the results.

The negative sign in Equation 1 ensures that the final velocities (which point into the detector) are antiparallel to the sector's look directions $\vec{l}$ (which point radially outward). At every node $\vec{r}_f$ along the spacecraft trajectory, an individual ion macroparticle is launched for each of the $17N = 5100$ unique combinations of possible longitude θ_v, latitude ϕ_v, and energy $E_{f,\mathrm{NH}}$. Equation 1 yields velocity vectors $\vec{v}'_{f,\mathrm{NH}}$ in the (x', y', z') coordinate system. For an arbitrary orientation of the FOV, the axes of this system are rotated against the basis vectors $\{\vec{e}_x, \vec{e}_y, \vec{e}_z\}$ of the Σ_{NH} frame. Expressing the components of the $\vec{v}'_{f,\mathrm{NH}}$ vectors with this basis yields the ions' final velocities $\vec{v}_{f,\mathrm{NH}}$ in the Σ_{NH} frame.

2.3. Tracing Energetic Ions Through Pluto's Induced Magnetosphere

The energetic He^+ ions are traced in the Pluto rest frame Σ_{P}, that is, the same frame in which AIKEF calculates a steady-state "snapshot" of the electromagnetic fields (see also Ruch et al., 2025). Thus, the final velocity vectors

$\vec{v}_{f,\mathrm{NH}}$, which define the *starting* conditions for *back*tracing, must be transformed from the NH rest frame Σ_{NH} into Σ_{P}:

$$\vec{v}_{f,\mathrm{P}} = \vec{v}_{f,\mathrm{NH}} + \vec{u}_{\mathrm{NH}} \quad , \tag{2}$$

where $\vec{v}_{f,\mathrm{P}}$ represents an ion's final velocity vector in the Σ_{P} frame. The constant vector $\vec{u}_{\mathrm{NH}} = (13.3, -3.5, 0.7)$ km/s is the average spacecraft velocity in the Σ_{P} frame across the entire day of the flyby: the instantaneous velocity of the spacecraft varied in magnitude by less than 1% throughout this period. Notably, its speed $|\vec{u}_{\mathrm{NH}}|$ is an order of magnitude smaller than the speed of the ambient solar wind $|\vec{u}_{\mathrm{SW}}|$.

The ions' trajectories in Σ_{P} are calculated by solving the non-relativistic equations of motion for a charged particle in electromagnetic fields. At the highest energies we consider, the relativistic mass growth of an He^+ ion is by less than 0.01%, so a classical treatment is appropriate. The method employed for tracing an ion's trajectory depends on its instantaneous position within the model domain (analogous to Ruch et al., 2025). While inside the AIKEF box, where the fields are non-uniform, a Runge-Kutta scheme of fourth order accuracy is used to numerically solve for the particle's position and velocity. The timestep for backtracing is $\Delta t = -2.5 \cdot 10^{-4}\, \Omega_0^{-1}$, where $\Omega_0 = \frac{e|\vec{B}_0|}{m}$ is the gyrofrequency of He^+ in the unperturbed solar wind field $\vec{B}_0$. Outside of the AIKEF box, where the fields are treated as uniform ($\vec{E}_0$ and $\vec{B}_0$), the particles' position and velocity (as a function of time) can be expressed analytically. In constant electromagnetic fields, the trajectories for moving *forward* in time, given arbitrary *initial* conditions, are described by Equations 6 and 7 in Ruch et al. (2025). When tracing the particles *backward* in time, the initial conditions appearing in these equations are substituted for the particle's position and velocity at the moment of transition from the perturbed fields inside the AIKEF domain to the uniform fields outside. If the trajectory of a backtraced ion transitions from uniform fields back into the AIKEF box, its motion is again calculated by the Runge-Kutta routine.

Particles are traced backward in time until they pass through the plane at $x = -762\ R_P$ upstream of Pluto. This large distance ensures that even He^+ ions at the highest energies considered (gyroradii $\sim 10^2\ R_P$) will not be able to gyrate back into the perturbed field region after crossing this plane. Such ions are considered to have "escaped" Pluto's induced magnetosphere. The velocity $\vec{v}_{i,\mathrm{P}}$ of a particle (in Σ_{P}) as it passes through this "escape plane" is recorded, and this vector is then transformed into the solar wind frame Σ_{SW}:

$$\vec{v}_{i,\mathrm{SW}} = \vec{v}_{i,\mathrm{P}} - \vec{u}_{\mathrm{SW}}, \tag{3}$$

where $\vec{v}_{i,\mathrm{SW}}$ is the velocity vector in Σ_{SW}. We use the subscript i ("initial") to refer to the velocity of escaped He^+ macroparticles (see also Table 1). While reaching the escape plane far upstream of Pluto constitutes the end of the backtracing process, particles would begin their motion in the upstream region with initial velocity vectors $\vec{v}_{i,\mathrm{SW}}$ (or $\vec{v}_{i,\mathrm{P}}$) when moving forward in time. The transformation to Σ_{SW} is necessary for determining the differential intensity an ion carries into the detector (see Section 2.4); our approach ensures that the flux assigned to an ion does not depend on the gyrophase it possesses as it reaches the escape plane (see Section 2.4.1).

Alternatively, the trajectory of a backtraced ion may intercept Pluto or its collisional atmosphere before reaching the escape plane. In the forward-tracing picture, such an ion would have to pass through the obstacle in order to reach the detector downstream. Thus, ions with such trajectories are removed from the simulation, contributing no flux into the detector (analogous to, e.g., Tippens, Roussos, et al., 2024; Tippens, Simon, & Roussos, 2024; Haynes, Tippens, et al., 2025; Haynes, Simon, & Liuzzo, 2025). However, Pluto's exobase is located near 1.36 R_P altitude (Gladstone et al., 2016), which is only a small fraction of the He^+ gyroradii. Therefore, less than $\sim$1% of He^+ ions in each simulation have such a fate.

2.4. Determining the Energetic Ion Flux Into the Detector

2.4.1. The Differential Intensity Carried by a Macroparticle

The differential intensity $I_{f,\mathrm{NH}}$ (in units of $\mathrm{cm}^{-2}\ \mathrm{s}^{-1}\ \mathrm{keV}^{-1}\ \mathrm{sr}^{-1}$) carried by a single ion macroparticle as it enters the PEPSSI detector (at the "starting point" of the backtracing procedure) is calculated using Liouville's theorem (e.g., Haynes, Tippens, et al., 2025; Ruch et al., 2025; Tippens, Roussos, et al., 2024):

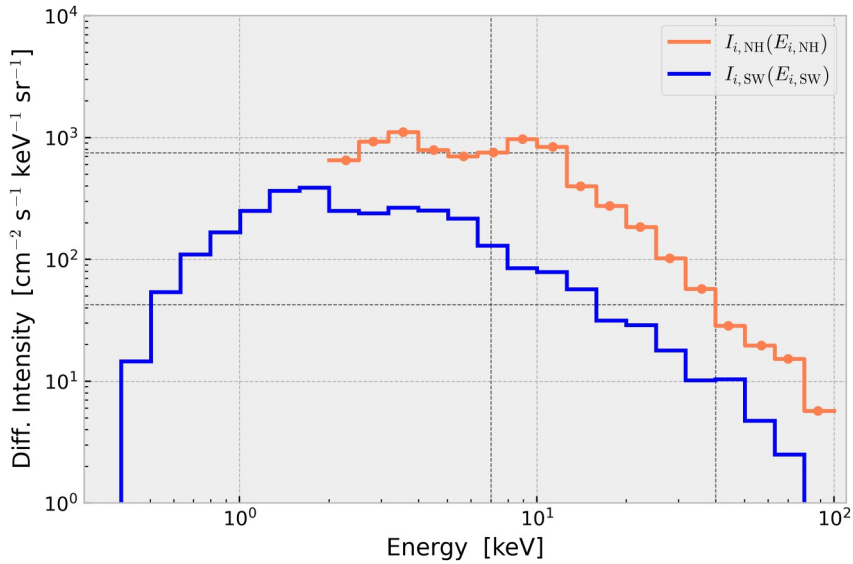

Figure 3. Ion energy spectra in the unperturbed solar wind 200 R_P upstream of Pluto. The orange curve shows the observed $I_{i,\mathrm{NH}}(E_{i,\mathrm{NH}})$ spectrum in the rest frame of the spacecraft, Σ_{NH}, with orange dots representing the data from Kollmann, Hill, Allen, et al. (2019). The $I_{i,\mathrm{SW}}(E_{i,\mathrm{SW}})$ spectrum (blue) is the transformation of the orange curve into the solar wind frame Σ_{SW} (see Appendix A). The horizontal axis shows the energy of the ions in the respective frame: $E_{i,\mathrm{SW}}$ for the Σ_{SW} frame and $E_{i,\mathrm{NH}}$ for the Σ_{NH} frame. The dashed black lines are guides for sampling the $I_{i,\mathrm{NH}}(E_{i,\mathrm{NH}})$ spectrum as an approximation for the $I_{i,\mathrm{P}}(E_{i,\mathrm{P}})$ spectrum at energies $E_{i,\mathrm{P}} = 7$ keV and $E_{i,\mathrm{P}} = 40$ keV (see discussion in Section 2.4.1).

$$I_{f,\mathrm{NH}} = I_{i,\mathrm{SW}} \frac{E_{f,\mathrm{NH}}}{E_{i,\mathrm{SW}}}, \tag{4}$$

where $E_{i,\mathrm{SW}} = \frac{1}{2} m |\vec{v}_{i,\mathrm{SW}}|^2$ is the ion's energy when reaching the escape plane, expressed in the Σ_{SW} frame. The quantity $I_{i,\mathrm{SW}}$ is the differential intensity assigned to the ion in Σ_{SW} at the escape plane (i.e., at the end of the backtracing process). Figure 3 shows the $I_{i,\mathrm{NH}}(E_{i,\mathrm{NH}})$ spectrum for He^+ (orange) from Kollmann, Hill, Allen, et al. (2019), as measured by PEPSSI far upstream of Pluto. As shown in that study, the experimental errors of that data set are minimal (compared to the absolute values) and can safely be discarded. Analogous to Ruch et al. (2025), we treat the observed upstream distribution as spatially uniform, that is, it is assumed to be representative of the energetic He^+ fluxes at any point within the escape plane. The $I_{i,\mathrm{SW}}(E_{i,\mathrm{SW}})$ spectrum (blue) is the transformation of $I_{i,\mathrm{NH}}(E_{i,\mathrm{NH}})$ into the Σ_{SW} frame. The method used to transform this data set from Σ_{NH} to Σ_{SW} and obtain $I_{i,\mathrm{SW}}(E_{i,\mathrm{SW}})$ is discussed in Appendix A. To determine the value of $I_{i,\mathrm{SW}}$ for a macroparticle, the observed spectrum in the Σ_{SW} frame is sampled at the ion's energy $E_{i,\mathrm{SW}}$. This process also takes into account that, in Σ_{SW}, the velocity distribution of energetic heliospheric ions is seen to be isotropic at a given energy (e.g., Kollmann, Hill, McNutt, et al., 2019). Following this procedure, all three quantities on the right side of Equation 4 are known, and we can determine the differential intensity $I_{f,\mathrm{NH}}$ carried by an individual macroparticle into the detector.

In our model setup, it is imperative that we sample the upstream energy spectrum in the Σ_{SW} frame that is *at rest* with respect to the unperturbed solar wind. For example, in the Σ_{P} frame, ions in the uniform fields upstream of Pluto ($\vec{E}_0$, $\vec{B}_0$) drift perpendicular to $\vec{B}_0$ with the bulk velocity of the solar wind, $(\vec{E}_0 \times \vec{B}_0)/|\vec{B}_0|^2 = \vec{u}_{\mathrm{SW}}$, in addition to their gyration around and translation along $\vec{B}_0$. Only in the Σ_{SW} frame does the drift disappear, such that an ion's energy $E_{i,\mathrm{SW}}$ is constant throughout a gyration. In any reference frame that moves with constant velocity relative to Σ_{SW}, the drift motion causes an ion's energy to vary with its gyrophase (see also Ruch et al., 2025). In such a frame, the sampled differential intensity of an ion macroparticle would then depend on the x-position of our escape plane: moving this plane would change the gyrophase at which the ion trajectory intersects it. In the Σ_{P} frame, an He^+ ion drifts a distance of $\Delta x = |\vec{u}_{\mathrm{SW}}| P_0 = 371\ R_P$ over a single gyroperiod, $P_0 = 2\pi\,\Omega_0^{-1}$, so its gyrophase (and hence, its energy) varies across this distance.

As an example, we consider an He^+ ion with a 90° pitch angle and an energy of $E_{i,\mathrm{SW}} = 20$ keV in the solar wind frame Σ_{SW}. Such a particle's energy in the Pluto frame Σ_{P} varies between $E_{i,\mathrm{P}} = 7$ keV (when gyrating opposite the drift direction) and $E_{i,\mathrm{P}} = 40$ keV (when gyrating in the drift direction) across the distance Δx. For ions in the keV regime, the speed of the spacecraft ($|\vec{u}_{\mathrm{NH}}| = 13.8$ km/s) is much lower than their gyration speeds ($\gtrsim$300 km/s). Thus, for this example, we will use the $I_{i,\mathrm{NH}}(E_{i,\mathrm{NH}})$ spectrum in the Σ_{NH} frame (orange, Figure 3) as an approximation for the $I_{i,\mathrm{P}}(E_{i,\mathrm{P}})$ spectrum in the Σ_{P} frame. Sampling the spectrum in Σ_{P} (instead of Σ_{SW}) at the two energy extrema reveals over an order of magnitude uncertainty in the ion's assigned differential intensity across a gyration (see dashed black guides, Figure 3): $I_{i,\mathrm{P}}(40\ \mathrm{keV}) \approx \frac{1}{18} I_{i,\mathrm{P}}(7\ \mathrm{keV})$. Hence, if we instead used the ion's energy in Σ_{P} (or Σ_{NH}) to determine its intensity upstream, the result could vary by more than a factor of 10 depending on our choice for the location of the escape plane. This model uncertainty is comparable in magnitude to the effect we seek to explain, namely a drop in the He^+ fluxes observed downstream by about an order of magnitude. Therefore, sampling the energy spectrum in the Σ_{SW} frame is the only way to avoid any uncertainty introduced by the placement of our escape plane.

This feature of our model constitutes a major difference from backtracing simulations of energetic magnetospheric ions at Titan or the Galilean moons of Jupiter: these particles typically possess drift velocities that are much smaller than the speed of their gyration or translation. Hence, in these environments, the particles' energies remain approximately constant over a gyroperiod, even when their drift motion is included. For this reason, backtracing models of energetic ion dynamics at these moons usually do not face such ambiguities when defining their "escape" criteria (e.g., Addison et al., 2021; Addison et al., 2022, 2023; Nordheim et al., 2022; Tippens, Roussos, et al., 2024).

2.4.2. The Total Differential Intensity Observed by the Detector

To calculate the differential intensity $\mathcal{I}$ represented by *all* ions that enter the detector at a certain node $\vec{r}_f$ for a given energy $E_{f,\mathrm{NH}}$, we first determine the contribution from each individual macroparticle launched antiparallel to look directions $\vec{l}\,(\theta_v, \phi_v)$ within the FOV. The angular discretization of the sector's FOV (Section 2.2) divides it into N surface area elements A^λ (individual grid cells in Figure 2) with latitude θ_v^λ:

$$A^\lambda = r_{\mathrm{inst}}^2 \cos\theta_v^\lambda\, \delta\theta_v\, \delta\phi_v, \qquad \text{where} \quad \lambda = 1, 2, \ldots, N. \tag{5}$$

The upper index "λ" refers to both the surface area element A^λ and the single macroparticle that passes through it with velocity vector $\vec{v}_{f,\mathrm{NH}}$ described by θ_v^λ and ϕ_v^λ. The quantity $r_{\mathrm{inst}} \approx 3$ cm is the radial distance from the center of the detector to the entrance at which ions are accepted (McNutt et al., 2008). Because of the dependence on θ_v^λ, surface area elements A^λ at higher detector latitudes are smaller than those closer to the $z' = 0$ plane. The total surface area A of the detector is given by

$$A = r_{\mathrm{inst}}^2 \int_{-\frac{\Delta\phi_v}{2}}^{+\frac{\Delta\phi_v}{2}} \int_{-\frac{\Delta\theta_v}{2}}^{+\frac{\Delta\theta_v}{2}} \cos\theta_v\, \mathrm{d}\theta_v\, \mathrm{d}\phi_v \approx \sum_{\lambda=1}^{N} A^\lambda. \tag{6}$$

Given the differential intensity $I_{f,\mathrm{NH}}^\lambda$ carried by macroparticle λ into the detector element A^λ, the number of real ions per time (per keV, per sr) passing through that element is given by $A^\lambda I_{f,\mathrm{NH}}^\lambda$. The differential intensity across the entire detector, contributed solely by macroparticle λ, is then determined by redistributing $A^\lambda I_{f,\mathrm{NH}}^\lambda$ across the detector's total surface area: $\frac{A^\lambda}{A} I_{f,\mathrm{NH}}^\lambda$. Hence, the differential intensity $\mathcal{I}$ measured by the detector for a given final energy $E_{f,\mathrm{NH}}$ at a certain node $\vec{r}_f$ is obtained by taking the sum over all macroparticles:

$$\mathcal{I} = \sum_{\lambda=1}^{N} \frac{A^\lambda}{A} I_{f,\mathrm{NH}}^\lambda = \sum_{\lambda=1}^{N} \frac{\cos\theta_v^\lambda\, \delta\theta_v\, \delta\phi_v}{\int_{-\Delta\phi_v/2}^{+\Delta\phi_v/2} \int_{-\Delta\theta_v/2}^{+\Delta\theta_v/2} \cos\theta_v\, \mathrm{d}\theta_v\, \mathrm{d}\phi_v} I_{f,\mathrm{NH}}^\lambda. \tag{7}$$

The factor of r_{inst}^2 in the expressions for A^λ and A (Equations 5 and 6) leads their ratio to be independent of r_{inst}.

In the (hypothetical) case where each surface element has the same area A^λ, the "weight" of each macroparticle's contribution reduces to $A^\lambda/A = 1/N$, and Equation 7 can be written as

$$\mathcal{I} = \frac{1}{N}\sum_{\lambda=1}^{N} I^\lambda_{f,\mathrm{NH}} \quad . \tag{8}$$

Although the areas of the individual surface elements A^λ depend on $\cos\theta_v^\lambda$, the minimum value of A^λ differs from the maximum by only 0.5% since this angle covers a small range of $\theta_v \in (-6°, 6°)$. Thus, we can use Equation 8 as a reasonable approximation for $\mathcal{I}$ in our model. In other words, the signal captured by PEPSSI at a certain position $\vec{r}_f$ (and for a certain energy $E_{f,\mathrm{NH}}$) becomes the average of the intensities carried by all backtraced macroparticles λ into the FOV. The individual contributions $I^\lambda_{f,\mathrm{NH}}$ are obtained by sampling the observed upstream spectrum $I_{i,\mathrm{SW}}(E_{i,\mathrm{SW}})$ for each particle and using Equation 4.

If we instead calculated $\mathcal{I}$ by merely taking the sum of all $I^\lambda_{f,\mathrm{NH}}$ (i.e., neglecting the $1/N$ factor in Equation 8), launching $2N$ macroparticles per energy at node $\vec{r}_f$ instead of N (e.g., by halving the value of $\delta\theta_v$) would roughly double the value of $\mathcal{I}$. However, since Equation 8 weights each macroparticle by the relative area of the associated surface element, the total differential intensity $\mathcal{I}$ does not scale with our arbitrary choice of N.

2.5. Viewing Geometries for a Spacecraft Detector

While NH conducted only a single Pluto flyby, we consider multiple spacecraft trajectories through the dwarf planet's induced magnetosphere for constructing synthetic time series of energetic He^+ flux into sector S0. This includes the actual path of the NH spacecraft, plus three hypothetical, idealized trajectories. In this way, we can provide context for our analysis by targeting regions of Pluto's induced magnetosphere that were not (or only briefly) sampled by NH. Figure 4 illustrates projections of the four considered paths onto each coordinate plane of Σ_P. The segment of the NH trajectory ("NH", gray) that we consider starts at about $x = -250\ R_P$ upstream of Pluto and ends at $x = 200\ R_P$ downstream, comfortably encompassing the period across which the depletion in He^+ flux was observed (indigo segment of the trajectory; Kollmann, Hill, Allen, et al., 2019). In the model, the nodes $\vec{r}_f$ along this trajectory are displaced in intervals of 60 s. Hence, for a spacecraft moving with an approximately constant speed $|\vec{u}_\mathrm{NH}| = 13.8$ km/s in the Pluto frame Σ_P, adjacent nodes lie equal distances of about $|\Delta\vec{r}_f| = 0.7\ R_P$ apart.

With the three idealized spacecraft trajectories (labeled "P1", "P2", and "P3"), we can further examine the pattern in energetic ion fluxes found by Ruch et al. (2025): a region of depleted flux in the north, accompanied by an enhancement to the south. Each of these trajectories is placed at $x = 50\ R_P$ downstream, passing through the center of the region where NH observed the reduction in He^+ flux (between $x = 20\ R_P$ and $x = 80\ R_P$). The P1 (red) and P2 (green) paths are at $z = \pm 10\ R_P$, respectively; they are both parallel to the y-axis and the (hypothetical) spacecraft moves from $y = -200\ R_P$ to $y = 200\ R_P$. The P3 (blue) path is at $y = 0$ and parallel to the z-axis, moving northward from $z = -200\ R_P$ to $z = 200\ R_P$. This trajectory intersects both the enhancements and reductions in He^+ flux found with the planar detector in our preceding study (Ruch et al., 2025). The velocity of the hypothetical spacecraft for each of these three paths is determined by rotating $\vec{u}_\mathrm{NH}$ in the direction of travel: along $+\vec{e}_y$ for P1 and P2, and along $+\vec{e}_z$ for P3. The nodes along each of these hypothetical paths are also evenly spaced in intervals of 60 s, corresponding to a distance of $|\Delta\vec{r}_f| = 0.7\ R_P$.

For the NH trajectory, we first consider the actual orientation of sector S0's FOV which was changing in time; the instantaneous direction of the boresight $\vec{L}$ is represented by intermittent vectors attached to the gray trajectory in Figure 4. During the period in which the reduced He^+ fluxes were observed, the boresight's angle against the Sun-Pluto line stayed constant at 34° for a few hours. Additionally, we consider six idealized scenarios for the NH trajectory, in which the boresight $\vec{L}$ of sector S0 has a fixed orientation throughout the entire interval: $-\vec{e}_x$ (toward upstream), $+\vec{e}_x$ (toward downstream), $-\vec{e}_y$ (antiparallel to Pluto's orbital motion), $+\vec{e}_y$ (parallel to Pluto's orbital motion), $-\vec{e}_z$ (southward), and $+\vec{e}_z$ (northward). The detector's azimuth is oriented horizontally in the cases when $\vec{L}$ is parallel to the $z = 0$ plane (i.e., $\vec{L} \parallel \{-\vec{e}_x,\ +\vec{e}_x,\ -\vec{e}_y,\ +\vec{e}_y\}$); in the two other scenarios, it is aligned with $\vec{e}_y$. This approach allows us to constrain the detectability of deflected He^+ ions for a given orientation of $\vec{L}$. The six idealized look directions are also used for each of the three hypothetical spacecraft trajectories (P1, P2, P3).

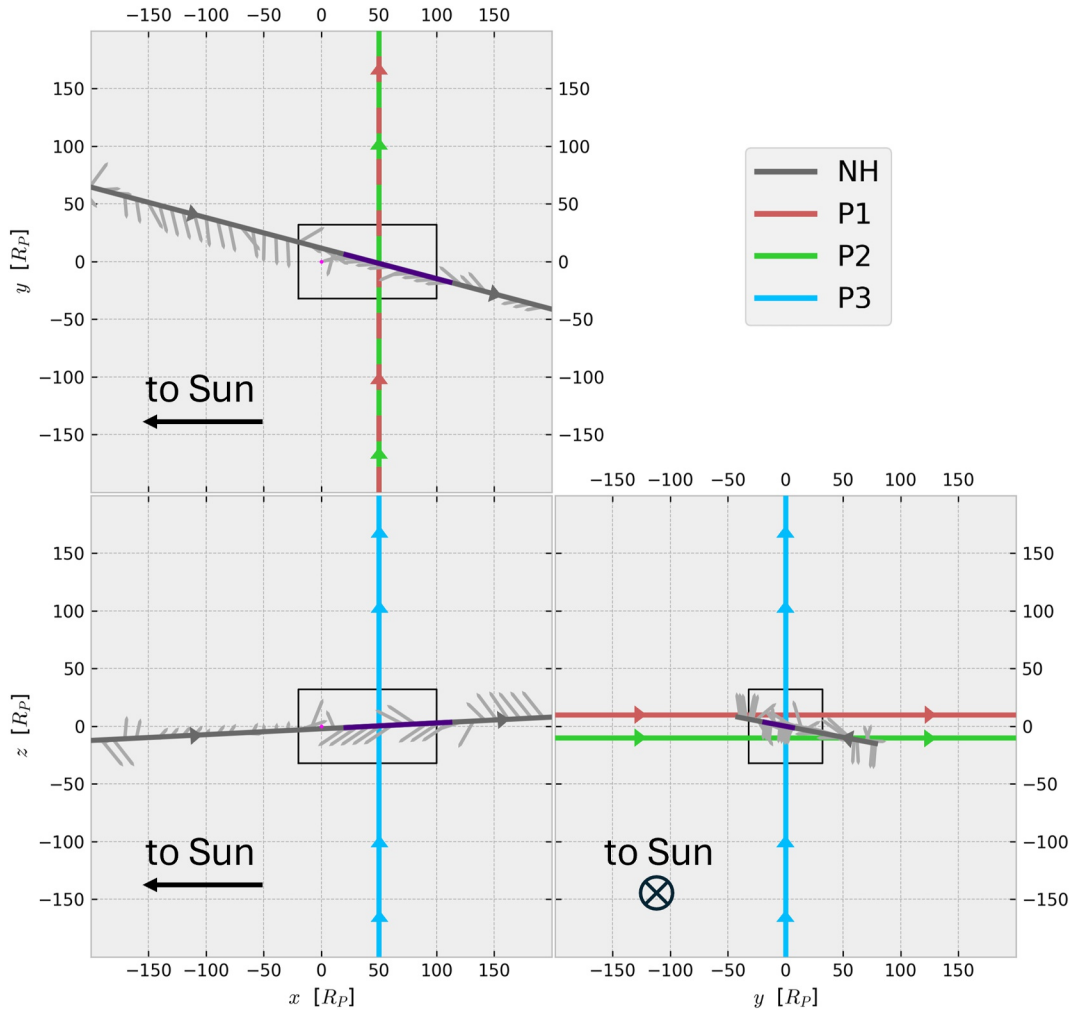

Figure 4. Schematic of the New Horizons (NH) trajectory and the three hypothetical spacecraft trajectories used to produce synthetic time series of the energetic ion flux, projected onto the $x = 0$, $y = 0$, and $z = 0$ planes of Σ_P. In dark gray is the actual trajectory of NH through the Pluto system. It is adorned with similarly colored vectors illustrating the momentary direction of the boresight for Pluto Energetic Particle Spectrometer Science Investigation sector S0. The indigo segment of the NH trajectory illustrates the region in which the reduction in He^+ flux was observed while the sector had a look direction 34° from the Sun-Pluto line. The P1 (red: $x = 50\ R_P$, $z = 10\ R_P$), P2 (green: $x = 50\ R_P$, $z = -10\ R_P$), and P3 (blue: $x = 50\ R_P$, $y = 0\ R_P$) trajectories are idealized (hypothetical) paths for the spacecraft that we also consider. The extent of the hybrid model domain is illustrated by the black rectangles, and the pink dot indicates the position of Pluto. Since the hypothetical trajectories are each parallel to one of the coordinate axes, they cannot be projected into the plane perpendicular to the spacecraft's path. Hence, they are not shown in those respective panels.

Hence, our study takes into account 24 individual combinations of spacecraft trajectory and look direction in addition to the actual instrument bearings of NH during the flyby. Model results are shown for a subset of these geometries, namely those that provide the most meaningful physical insights.

The instantaneous orientation of the PEPSSI detector within the Σ_P frame, as well as NH's position and velocity during the flyby are calculated using the "SPICE" tool kit (Acton, 1996; Acton et al., 2018) and the corresponding kernels for the NH mission from the Planetary Data System (Steffl et al., 2010).

3. Modeling Results

3.1. Detectability of Energetic He^+ Along Idealized Spacecraft Trajectories

Figure 5 shows the synthetic differential intensity $\mathcal{I}$ of He^+ for each of the 17 considered energies $E_{f,\mathrm{NH}}$ along the P1 trajectory, located at $x = 50\ R_P$ and $z = 10\ R_P$. They are displayed as a function of the (hypothetical) spacecraft's y-coordinate in the Σ_P frame. Panels (a)–(d) give the results for an instrument with boresight $\vec{L}$ pointing in the $-\vec{e}_x$, $+\vec{e}_x$, $-\vec{e}_z$, and $+\vec{e}_z$ directions, respectively. The $\pm\vec{e}_y$ directions are not shown since the modeled fluxes into the detector are nearly uniform. At each considered energy $E_{f,\mathrm{NH}}$, we refer to the uniform value of $\mathcal{I}$ far from the interaction region as the "baseline", representing the unperturbed differential intensity in the ambient solar wind.

For a detector looking toward upstream (panel 5(a)), synthetic time series are shown only at energies of $E_{f,\mathrm{NH}} = 7.1$ keV or higher. At the five discrete energies below, many backtraced ions reaching the upstream region have energies less than $E_{i,\mathrm{SW}} \approx 400$ eV. However, as evidenced by the transformed spectrum in Figure 3 (blue curve), there is no information available to determine $I_{i,\mathrm{SW}}(E_{i,\mathrm{SW}})$ at these lower energies (see also Appendix A). Since it is not feasible to construct the energy spectrum below $E_{i,\mathrm{SW}} \approx 400$ eV, no results are shown for the few energies $E_{f,\mathrm{NH}}$ affected by this lower cutoff for $I_{i,\mathrm{SW}}(E_{i,\mathrm{SW}})$.

Equation 4 elucidates why the detector facing downstream (panel 5(b)) observes the lowest baseline intensities among the considered look directions. This is the only detector that *requires* the He^+ ions to have a velocity component anti-parallel to their drift at some phase of their gyration in order to be captured. Hence, the minimum energy $E_{i,\mathrm{SW}}$ of such ions (in Σ_SW) is higher than for the other five look directions. In order to oppose the drift motion and travel toward upstream, an energy of at least $E_{i,\mathrm{SW}} = \frac{1}{2}m|\vec{u}_\mathrm{SW} - \vec{u}_\mathrm{NH}|^2 \approx 3.2$ keV is needed (in Σ_SW, but *not* in Σ_NH). As a result, the ions' energies are pushed farther to the right of the peak in the $I_{i,\mathrm{SW}}(E_{i,\mathrm{SW}})$ spectrum (blue curve, Figure 3) where the intensity decreases with energy, leading to lower baselines. On the other hand, the intensities when looking toward upstream (panel 5(a)) have the *greatest* baselines among the other look directions, since these ions entering the detector will have lower energies in the Σ_SW frame, near where $I_{i,\mathrm{SW}}(E_{i,\mathrm{SW}})$ is maximized (blue curve, Figure 3).

Across all boresight directions in Figure 5, the magnitude of the *perturbations* in differential intensity decreases with greater detection energy $E_{f,\mathrm{NH}}$, dropping below 50% of their respective baselines for $E_{f,\mathrm{NH}} \geq 11.3$ keV. This trend is consistent with the results of Ruch et al. (2025): it was shown that the influence of Pluto's induced magnetosphere on energetic ion trajectories diminishes for larger gyroradii, leading the amplitude of the perturbations in downstream flux to decrease at higher energies. Most importantly, Figure 5 shows that, for a finite field-of-view, the observable perturbations to the He^+ ion intensity are strongly dependent on the detector's look direction. Some orientations of $\vec{L}$ see deviations by less than 30% of the baseline even at the lowest energies, such as $+\vec{e}_x$ (panel 5(b)), $+\vec{e}_z$ (panel 5(d)), and $\pm\vec{e}_y$ (not depicted here). The observed interaction signatures in $\mathcal{I}$ are strongest when the boresight points southward (panel 5(c)): in this case, the modeled intensities exhibit a broad decrease from their baselines by up to a factor of two, but only at energies $E_{f,\mathrm{NH}} \leq 4.5$ keV (dark blue). Thus, along the P1 trajectory, the magnitude of the modeled perturbations in ion intensity for all six detector look directions remains significantly below that of the strongest depletion (factor of 10) observed by NH near Pluto. Notably, the P1 trajectory is $x = 50\ R_P$ downstream (as are P2 and P3), at which the observed He^+ flux had already roughly doubled following the initial order-of-magnitude depletion when NH was at $x \approx 20\ R_P$ (Kollmann, Hill, Allen, et al., 2019).

Figure 6 shows the modeled differential intensity for trajectories P2 and P3 (panels (a)–(b) and (c)–(d), respectively) with the detector pointing upstream ($-\vec{e}_x$) or southward ($-\vec{e}_z$). Results for the other four boresight directions are not depicted along either trajectory, since the modeled fluxes in these cases are nearly uniform. Similar to the P1 trajectory, the synthetic data sets exhibit perturbations that diminish with greater energy, becoming increasingly negligible for $E_{f,\mathrm{NH}} \geq 22.4$ keV (lime green). For the P2 trajectory (panels 6(a) and 6(b)), the differential intensities at $E_{f,\mathrm{NH}} \leq 7.1$ keV display a reduction by up to a factor of two inside the induced magnetosphere. For P3, the strongest perturbation is seen for the southward-facing detector ($-\vec{e}_z$) as a broad reduction in flux by up to a factor of three, stretched toward the north of Pluto's orbital plane ($z > 0$, panel 6(d)). This is consistent with the north-south asymmetry of the dwarf planet's induced magnetosphere across the $z = 0$

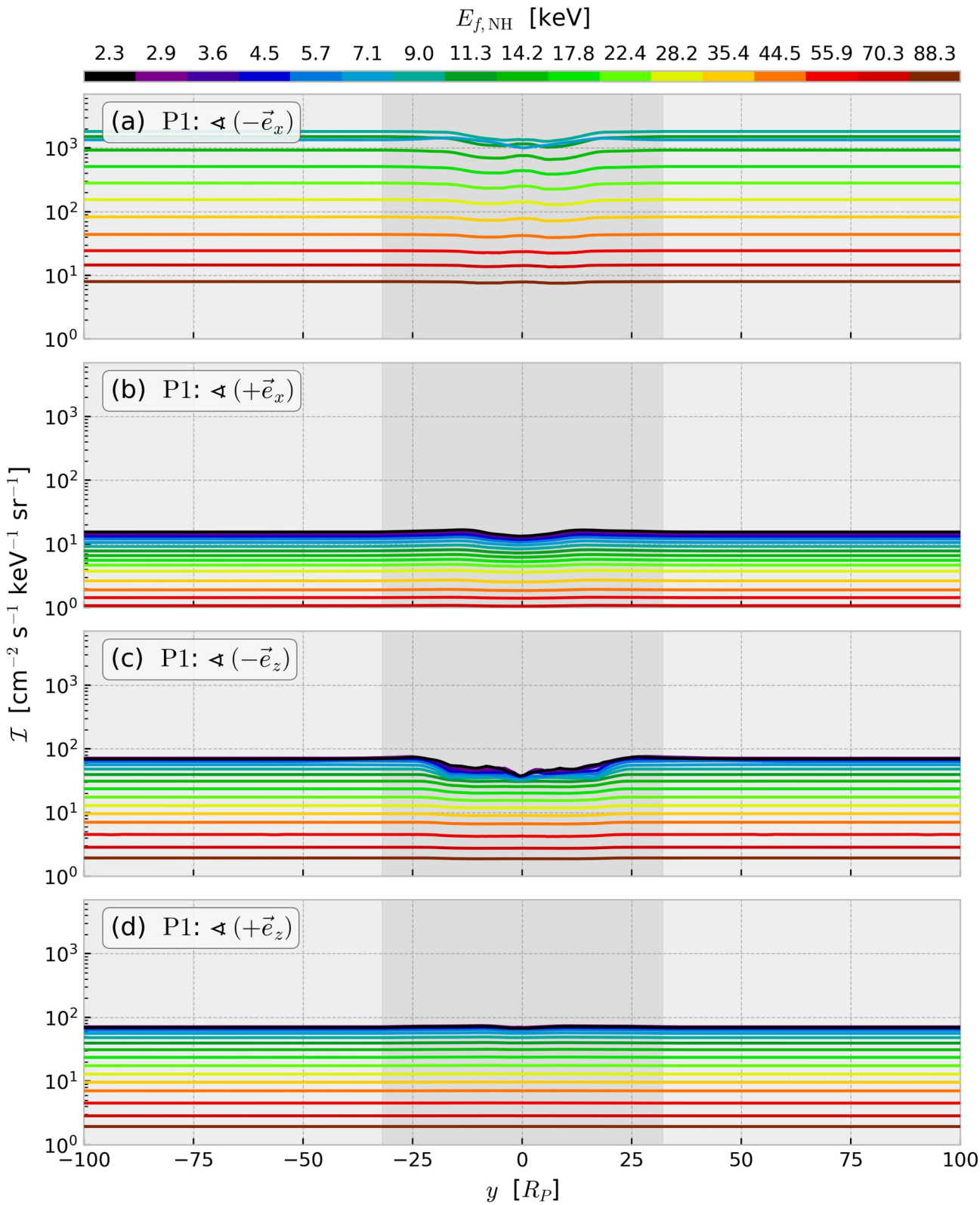

Figure 5. Synthetic time series of He^+ differential intensity $\mathcal{I}$ for the P1 spacecraft trajectory at ($x = 50\ R_P$, $z = 10\ R_P$). The horizontal axis plots the (hypothetical) spacecraft's y-position, since its path is parallel to the y-axis. The panels show the results for different, fixed detector look directions (◁): toward upstream (a), toward downstream (b), southward (c), and northward (d). Each colored line represents the ion intensity $\mathcal{I}$ for a certain detected energy $E_{f,\mathrm{NH}}$. The dark shaded region ($|y| \leq 32\ R_P$) indicates where the trajectory is within the AIKEF domain. In panel (a), no results are shown for the lowest five energies considered (see text for discussion).

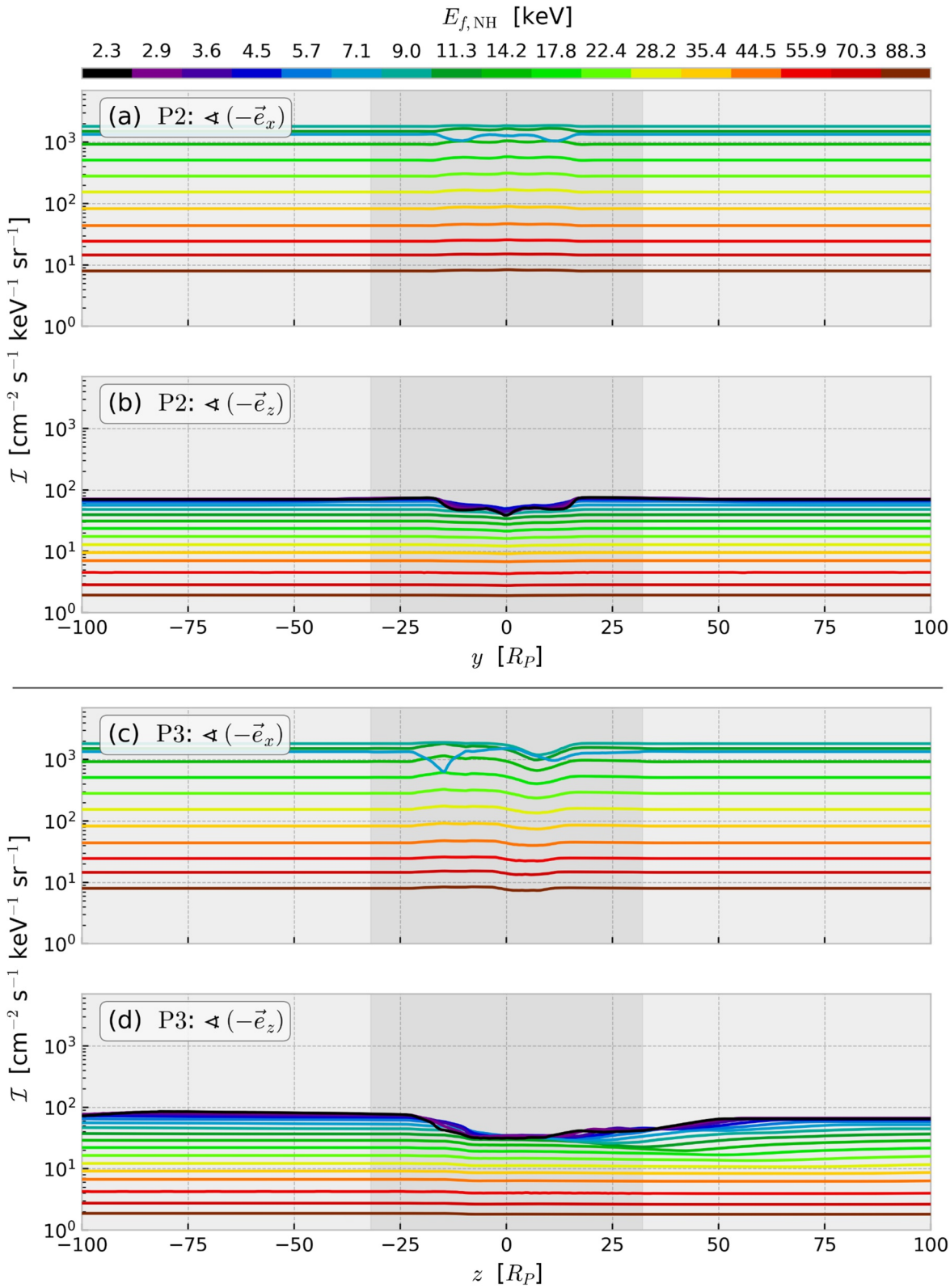

Figure 6.

plane (e.g., Delamere, 2009). For an opposite IMF orientation, $\vec{B}_0 \propto +\vec{e}_y$, these signatures would be mirrored at this plane. With either trajectory, at energies as high as $E_{f,\mathrm{NH}} \geq 35.4$ keV (yellow-orange), the ion intensities are nearly uniform throughout.

Analogous to P1, our results for the P2 and P3 trajectories demonstrate that the observable changes in He^+ flux vary drastically with the detector's orientation: even along the same spacecraft trajectory, the perturbations to the intensities vary between different look directions. Of the six considered boresight orientations, the detectors pointing upstream ($-\vec{e}_x$) and southward ($-\vec{e}_z$) are the only ones that display significant deviations from the baseline along all three synthetic trajectories. These look directions are closely aligned with that of sector S0 as it observed the factor-of-10 depletion in He^+ flux: it was tilted by 34° southward against $-\vec{e}_x$ (Kollmann, Hill, Allen, et al., 2019). Independent of the orientation of our model detector, the magnitude of the observed perturbations in ion intensity diminishes with increasing energy $E_{f,\mathrm{NH}}$, never reaching more than 30% of the baseline at energies $E_{f,\mathrm{NH}} \geq 22.4$ keV. Such an energy dependence is consistent with energetic ions dynamics at other small bodies, for example, Callisto (Liuzzo et al., 2019b) or Europa (Addison et al., 2021; Nordheim et al., 2022).

3.2. Detectability of Energetic He^+ Along the New Horizons Trajectory

3.2.1. Fixed Detector Look Directions

Figure 7 displays time series of the modeled differential intensity $\mathcal{I}$ along the actual trajectory of the NH flyby, but for the six idealized boresight $\vec{L}$ directions (panels (a)–(f)), as well as the evolution of the spacecraft's position with time (panel (g)). Panel (h) shows a colormap of the magnetic field strength within the AIKEF domain in the $z = 0$ plane. The bow shock is seen as the yellow-green outer boundary of the induced magnetosphere, and the magnetic pileup region as the red/orange region of elevated $|\vec{B}|$ upstream of Pluto. The colormap is overlain by a projection of the NH trajectory (black), which intersects this plane at ($x = 44\ R_P$, $y = 0\ R_P$) and forms an angle of less than 3° against it (see panel (g)). Just as in Figure 5, the "baseline" intensities far upstream of Pluto for $\vec{L} \propto -\vec{e}_x$ (panel 7(a)) exceed those seen at the other five boresight directions. The lowest baseline fluxes are again captured by the detector looking toward downstream (panel 7(b)). When observing along certain look directions, for example, $+\vec{e}_y$ (panel 7(d)), the ion intensities captured by the detector are nearly uniform regardless of energy $E_{f,\mathrm{NH}}$.

Along the NH trajectory, the most extended depletions in differential intensity are visible for a detector looking southward (panel 7(e)). In this case, detected energies $E_{f,\mathrm{NH}} \leq 5.7$ keV each exhibit an abrupt decrease in flux by a factor of two starting around 12:00 UTC, shortly after closest approach (gray dashed line). The onset of this reduction coincides with the spacecraft crossing Pluto's bow shock and entering the induced magnetosphere (see panel 7(h)). The modeled He^+ differential intensities in panel 7(e) gradually increase out to $x \approx 100\ R_P$, qualitatively similar to the "refilling" that appears in observations by sector S0 in the same region (Kollmann, Hill, McNutt, et al., 2019).

For a detector looking toward upstream (panel 7(a)), an energy of $E_{f,\mathrm{NH}} = 5.7$ keV (blue) is the lowest value in Σ_{NH} that can occupy the spectrum constructed for Σ_{SW} above its 400 eV lower bound. At this energy, the modeled time series displays a broad flux enhancement by up to a factor of five after entry into Pluto's induced magnetosphere, extending as far as $x \approx 200\ R_P$ downstream. This signature is comparable in *magnitude* to the reduction seen by NH. The modeled enhancement largely stems from the non-monotonic shape of the $I_{i,\mathrm{SW}}(E_{i,\mathrm{SW}})$ spectrum (blue in Figure 3): when launched inside the induced magnetosphere at this value of $E_{f,\mathrm{NH}}$, the bulk of the backtraced ions samples the upstream distribution at energies $E_{i,\mathrm{SW}}$ around 1–2 keV. As can be seen from Figure 3, the highest intensities $I_{i,\mathrm{SW}}$ occur in this energy range. In contrast to this, backtraced ions launched at $E_{f,\mathrm{NH}} = 5.7$ keV *upstream* of Pluto's interaction region (i.e., earlier along the spacecraft trajectory for this look direction) would correspond to energies near $E_{i,\mathrm{SW}} \approx 0.5$ keV in Σ_{SW}, where the intensities given by

Figure 6. Synthetic time series of He^+ differential intensity for the idealized P2 (panels (a) and (b); $x = 50\ R_P$, $z = -10\ R_P$) and P3 (panels (c) and (d); $x = 50\ R_P$, $y = 0\ R_P$) trajectories, with detectors ($\prec$) pointed toward upstream ($\vec{L} \propto -\vec{e}_x$) or southward ($\vec{L} \propto -\vec{e}_z$). The horizontal axis plots the only coordinate that changes along each corresponding path. Colored lines show the differential intensity $\mathcal{I}$ for He^+ ions that enter the detector with a certain energy $E_{f,\mathrm{NH}}$. The dark shaded region indicates where the trajectory is within the AIKEF domain. In panels (a) and (c), no results are shown for the lowest five energies, analogous to Figure 5(a).

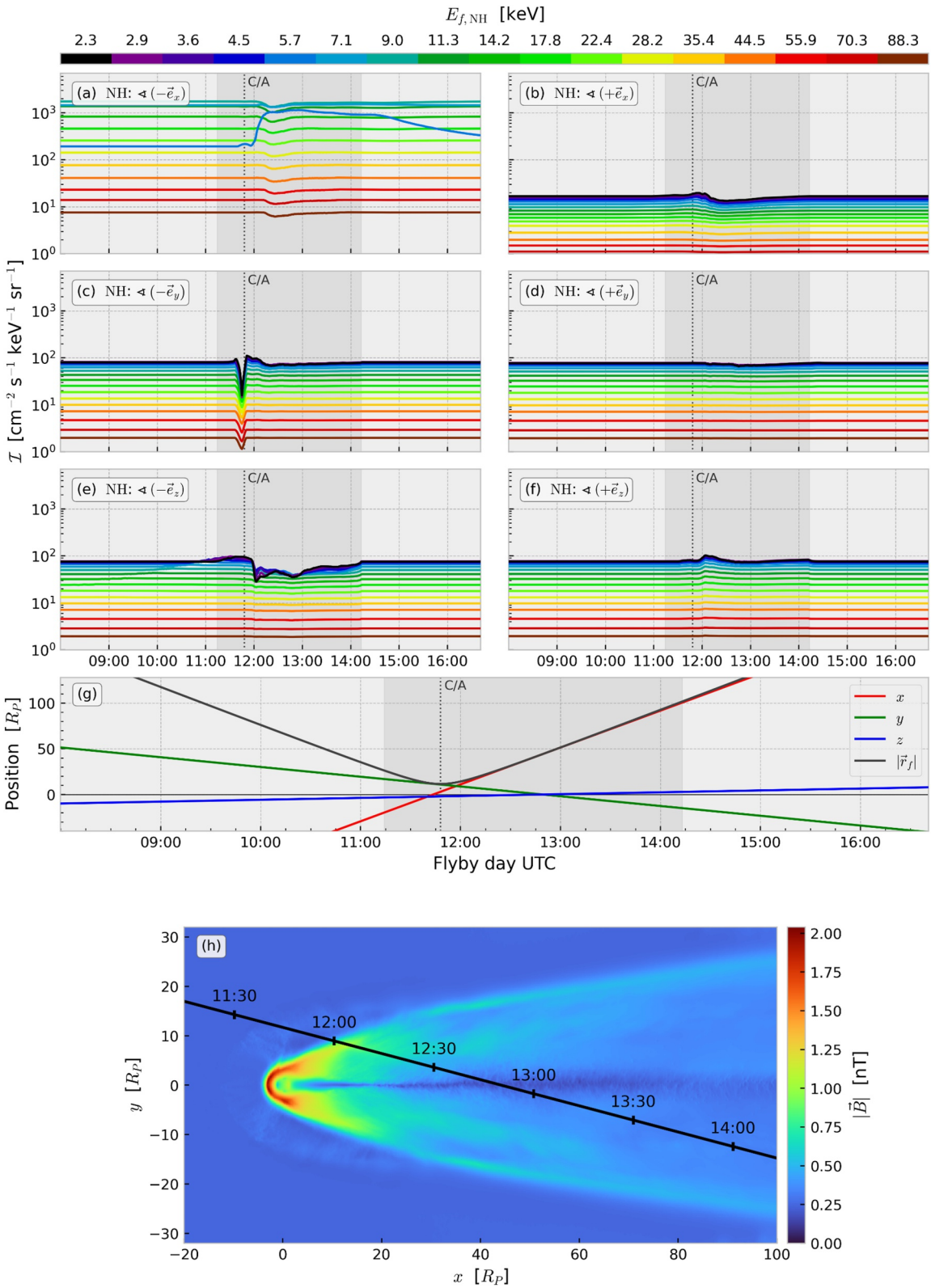

Figure 7.

the energy spectrum are lower. In other words, the $E_{f,\mathrm{NH}} = 5.7$ keV ions are accelerated near Pluto's bow shock; given the shape of the He^+ spectrum, this leads to an increase of their flux into the detector within the interaction region.

Simultaneous to the depletion in flux seen for a southward boresight (panel 7(e)), the detector looking northward (panel 7(f)) observes a slight enhancement in He^+ flux by up to 30% for these same energies. This disparity may stem from the ions' deflection by the perturbed fields within the induced magnetosphere (panel 7(h)). When traveling through, for example, the magnetic pileup region, an ion experiences a localized reduction in gyroradius as it spins around the component of $\vec{B}$ in the $-\vec{e}_y$ direction. For an ion whose velocity vector in this region points toward downstream, this decrease causes its trajectory to be deflected southward (see Figure 8(a) of Ruch et al., 2025). The northward-facing look direction of the detector in panel 7(f) is favorable for capturing such ions, leading to the slight enhancement in modeled fluxes shortly after closest approach. By the same token, ions that encounter the pileup region while moving northward along their gyration trajectory are deflected toward downstream by the reduction in gyroradius (see Figure 8b of Ruch et al., 2025). This prevents some of them from entering the southward-facing detector (panel 7(e)), contributing to the observed reduction in flux.

The detector pointing along $-\vec{e}_y$ (panel 7(c)) observes a brief depletion in He^+ intensity shortly before the spacecraft's passage through Pluto's bow shock. This event represents the sole instance of a decrease in modeled flux that is present at *all energies*. However, its magnitude still varies with $E_{f,\mathrm{NH}}$: the time series for the lowest considered energy ($E_{f,\mathrm{NH}} = 2.3$ keV) exhibits a factor of five decrease, whereas there is only a factor of two decrease at the upper end of our range ($E_{f,\mathrm{NH}} = 88.3$ keV). This depletion is the result of absorption by Pluto and its dense atmosphere. To illustrate this effect, Figure 8 shows the backtraced trajectories of several sample He^+ ions with energies $E_{f,\mathrm{NH}} = 2.3$ keV (purple) and $E_{f,\mathrm{NH}} = 88.3$ keV (pink). They are launched from the detector's position (white "◂") at the center of the observed depletion (11:45 UTC) and their paths are projected into the $x = 0$ and $z = 0$ planes of Σ_P (panels 8(a) and 8(b), respectively). The modeled depletion occurs only a dozen R_P away from Pluto, whereas ion gyroradii are up to $\sim 10^2$ R_P. At the same time, the chosen boresight is fixed in the direction of the dwarf planet. A different subset of ion trajectories is shown in each of the two panels: only ions with velocities $\vec{v}_{f,\mathrm{NH}}$ parallel to the respective plane are backtraced in either case. This is done such that paths of neighboring ions with the same energy do not visually obstruct one another. Ion trajectories at $E_{f,\mathrm{NH}} = 88.3$ keV are nearly straight, whereas ions at the lower end of our energy range experience stronger deflection by the elevated fields in the induced magnetosphere due their smaller gyroradii. In panel 8(a), each of the depicted trajectories at $E_{f,\mathrm{NH}} = 2.3$ keV (purple) intercepts Pluto's exobase (dashed black circle, ≈ 5 R_P diameter), but a few ions with $E_{f,\mathrm{NH}} = 88.3$ keV (pink) avoid absorption and pass through the weak field enhancement south of the dwarf planet. In panel 8(b), a few backtraced ions of both energies evade hitting the exobase: the "surviving" lower energy ions (purple) are deflected around Pluto's downstream side by the draped fields, whereas some of the higher energy particles (pink) narrowly avoid the dwarf planet by traveling south of it (perpendicular to the plane of the figure).

Many of the backtraced ions in Figure 8 have "forbidden" trajectories that intercept Pluto's exobase. As a result, these particles contribute no flux into the detector, leading to the depletion in Figure 7c across all energies. In the forward-tracing picture, such ions initially travel toward the detector but would be obstructed by Pluto's collisional atmosphere. Figure 8a suggests that the energy dependence in the magnitude of the flux depletion arises from the characteristics of the ions' trajectories: lower energy particles with smaller gyroradii are more susceptible to the perturbed fields and have a higher "risk" of hitting Pluto. At higher energies, this effect becomes less significant. Notably, this absorption-related depletion of He^+ flux into the detector was not sampled during the actual NH flyby (Section 3.2.2), since S0's boresight $\vec{L}$ never pointed directly toward Pluto.

Figure 7. Synthetic time series of He^+ differential intensity for the New Horizons (NH) spacecraft trajectory, but with a detector ("◂") whose boresight is fixed along idealized look directions: toward upstream (a), toward downstream (b), opposite to Pluto's orbital direction (c), along its orbital direction (d), southward (e), and northward (f). Colored lines show the differential intensity $\mathcal{I}$ for ions of a certain detected energy $E_{f,\mathrm{NH}}$. In panel (a), no results are shown for the lowest four energies, similar to Figure 5(a). Panel (g) plots the spacecraft's position and distance from Pluto's center in the Σ_P frame as a function of time. The dark shaded region indicates when the spacecraft is within the AIKEF domain; the vertical, dotted gray line marks its closest approach (C/A) to Pluto. The horizontal axis for each panel (a)–(g) gives UTC on the day of the flyby (14 July 2015). Panel (h) illustrates the magnetic field strength $|\vec{B}|$ within the AIKEF domain in the $z = 0$ plane (see Ruch et al., 2025). The black line indicates the NH trajectory, and it is adorned with markers giving the time at each position in increments of 30 min.

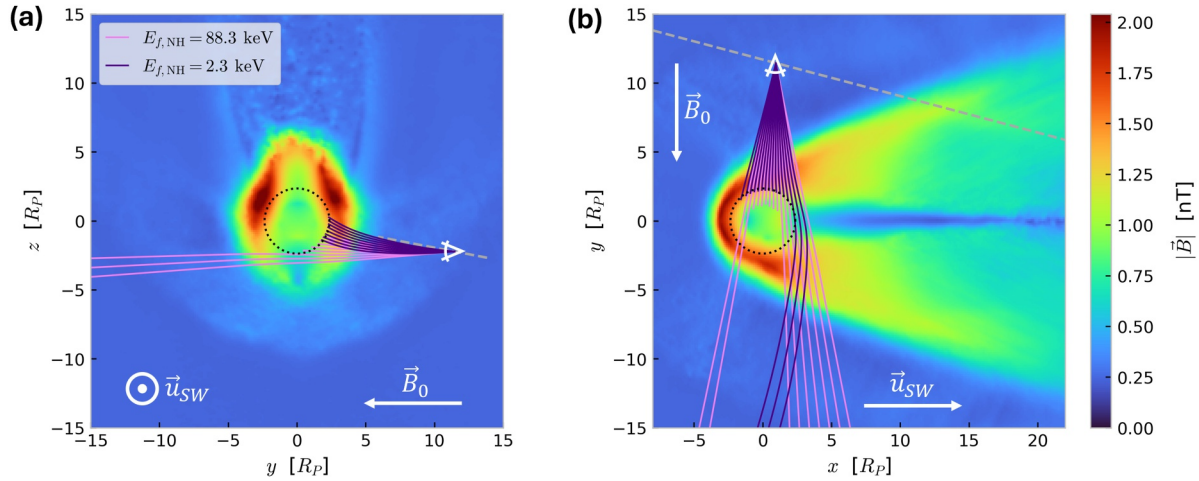

Figure 8. Sample backtraced He^+ trajectories (i.e., emanating from the detector) for energies $E_{f,\mathrm{NH}} = 2.3$ keV (purple) and $E_{f,\mathrm{NH}} = 88.3$ keV (pink), launched at the location of New Horizons at 11:45 UTC on the day of the Pluto flyby. The trajectories are projected into the $x = 0$ (panel (a)) and $z = 0$ (panel (b)) planes of Σ_P, overlain on top of a colormap of the magnetic field strength from AIKEF in the respective plane (see Ruch et al., 2025). To enhance visibility, the colors associated with the ion energies in this figure are different from those in the time series of, for example, Figure 7. The position and (hypothetical) orientation of the detector are indicated by the "◅" icon: its boresight is along $-\vec{e}_y$, corresponding to the idealized scenario in Figure 7(c). The two panels trace different sets of ions whose velocities $\vec{v}_{f,\mathrm{NH}}$ at launch are parallel to the respective plane: given the orientation of the detector's FOV about $\vec{L}$, this is the $\phi_v = 0°$ "slice" of ions in panel (a), and the $\theta_v = 0°$ "slice" in panel (b). For illustration purposes, the angular separations ($\delta\theta_v$, $\delta\phi_v$) between the discrete values of θ_v and ϕ_v have been increased by a factor of 1.5 compared to the actual model runs (see Section 2.2). The dashed gray line is the spacecraft's trajectory. Pluto's exobase (dashed black circle) is at 1.36 R_P altitude (Gladstone et al., 2016).

3.2.2. Time-Dependent Look Direction

Figure 9a shows the modeled time series of energetic He^+ differential intensities $\mathcal{I}$ using the *dynamic* look direction of sector S0 along the NH trajectory (Steffl et al., 2010) for all considered $E_{f,\mathrm{NH}}$. At low energies, the very few data points where ions would sample the upstream distribution below the observed energy range have been omitted (see also Appendix A). However, the absence of these points does not compromise the visibility of any features in panel 9(a). Panel 9(b) displays an averaged time series of the intensity carried into the detector by ions with energies $E_{f,\mathrm{NH}} \in \{11.3, 14.2, 17.8\}$ keV. These energies span the range of the L09 channel of sector S0 ($E_{f,\mathrm{NH}} \in [9.52, 18.00]$ keV); panel 9(c) plots the observations from this channel (see also Figure 1 of Kollmann, Hill, Allen, et al., 2019). We use an *average* of the ion intensities across these three energies (as opposed to a sum) to model the signal captured by the L09 channel (panel 9(b)) following the same logic as described in Section 2.4.2. The observable intensity should not depend on the number of $E_{f,\mathrm{NH}}$ values that we use to represent the L09 energy range. If we instead *summed* the time series obtained at discrete energies $E_{f,\mathrm{NH}}$, the intensity seen by our model detector would (artificially) grow if we increased the number of $E_{f,\mathrm{NH}}$ values within the range of channel L09.

Panels 9(d) and 9(e) illustrate the orientation of the detector's boresight $\vec{L}$ in Σ_P, described by the cone angle α and the clock angle β. Both quantities have been adopted from Kollmann, Hill, Allen, et al. (2019). The cone angle $\alpha \in [0°, 180°]$ defines the boresight's inclination against the $-\vec{e}_x$ direction (i.e., the Pluto-Sun line). Boresight vectors $\vec{L}$ with the same α form a *cone* around $-\vec{e}_x$ with opening angle 2α. A cone angle of $\alpha = 0°$ corresponds to the boresight pointing toward upstream ($-\vec{e}_x$), whereas $\alpha = 180°$ means that $\vec{L}$ points directly toward downstream ($+\vec{e}_x$). All boresight orientations perpendicular to $\vec{e}_x$ are characterized by $\alpha = 90°$.

For a given cone angle α, the *clock* angle $\beta \in [-180°, 180°]$ describes the orientation of the projection of $\vec{L} = (L_x, L_y, L_z)$ onto a plane spanned by $\vec{e}_y$ and $\vec{e}_z$ (i.e., perpendicular to the Pluto-Sun line). The clock angle is measured against the $+\vec{e}_z$ direction; it is positive for $L_y < 0$ and negative for $L_y > 0$. The value of this angle is $\beta = 0°$ when the projection of $\vec{L}$ points northward ($\propto +\vec{e}_z$) and $\beta = \pm 180°$ for a southward orientation ($\propto -\vec{e}_z$). For $\beta = \pm 90°$, the projected vector is aligned with $\mp\vec{e}_y$, respectively. The definitions of α and β are further illustrated in Figure 10.

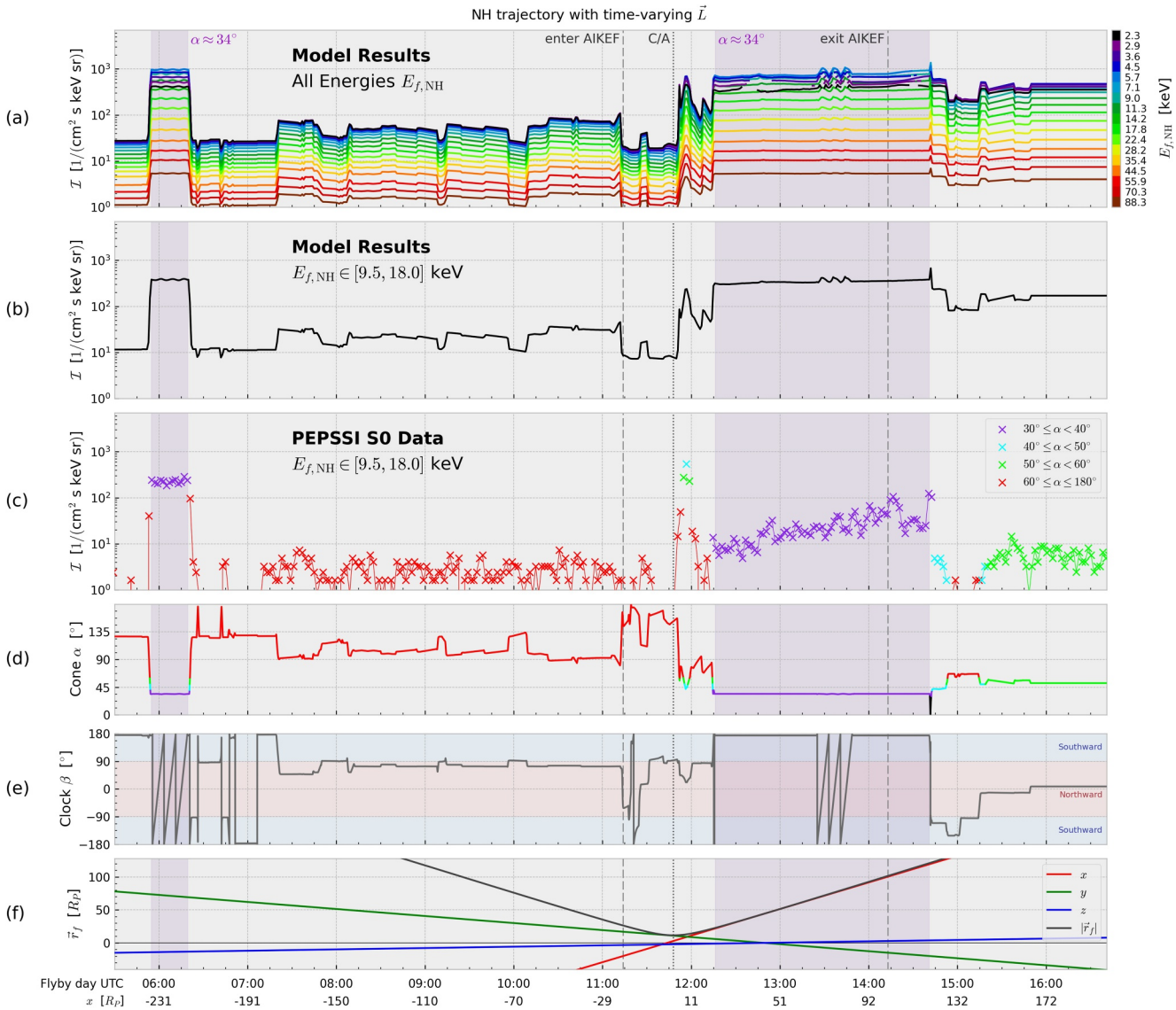

Figure 9. Modeled and observed energetic ion intensities along the New Horizons trajectory. Panel (a) displays the synthetic time series of He^+ differential intensity for each energy $E_{f,\mathrm{NH}}$, taking into account the time-dependent boresight orientation of sector S0. Panel (b) shows the modeled intensity for values of $E_{f,\mathrm{NH}}$ within the energy range of the L09 channel of sector S0 along the flyby trajectory ($E_{f,\mathrm{NH}} \in [9.5, 18.0]$ keV). This synthetic time series was obtained by averaging the intensities of ions with energies $E_{f,\mathrm{NH}} \in \{11.3, 14.2, 17.8\}$ keV. Panel (c) shows the *observed* He^+ intensity measured by sector S0 within the L09 channel's energy range (from Kollmann, Hill, Allen, et al., 2019). The data points are colored according to the value of the cone angle α at that given time. Panel (d) shows the cone angle α, describing the inclination of the detector's boresight $\vec{L}$ against the Pluto-Sun line. Panel (e) gives the clock angle β; the shaded red region indicates when $|\beta| < 90°$, such that the boresight points northward. The blue shaded regions in this panel correspond to $|\beta| > 90°$, for a boresight with a southward component. Panel (f) plots the spacecraft's position in Σ_P with time. In all panels, the vertical dotted line marks NH's closest approach (C/A) to Pluto. The times at which the spacecraft enters and exits the AIKEF domain are indicated by the vertical dashed lines. The two shaded purple regions near 06:00–06:15 UTC and 12:15–14:45 UTC in each panel highlight the regions of constant cone angle $\alpha \approx 34°$ used in our discussion.

The cone and clock angles are each seen to be non-uniform throughout the flyby (Figures 9d and 9e): the spacecraft was rotating to allow the remote sensing instruments to properly capture Pluto (e.g., Cheng et al., 2008; Stern et al., 2008). In general, the modeled and observed intensities $\mathcal{I}$ far upstream of the induced magnetosphere evolve in time as the detector orientation changes (panels 9(a)–(c)). For instance, the modeled values of $\mathcal{I}$ in that region (until at least 11:00 UTC) are greater for smaller cone angles α, corresponding to $\vec{L}$ pointing nearly toward upstream. Such behavior is consistent with that of the baselines in our model results from Figures 5–7, compared between the various idealized look directions.

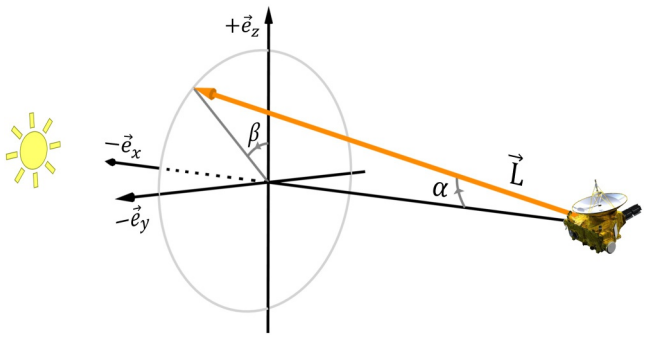

Figure 10. Diagram illustrating the definitions of the cone angle α and clock angle β for a given boresight vector $\vec{L}$ (orange). The cone angle α describes the inclination of $\vec{L}$ against the Pluto-Sun line ($-\vec{e}_x$). The clock angle β is the angle between the northward direction ($+\vec{e}_z$) and the projection of $\vec{L}$ onto a plane spanned by $\vec{e}_y$ and $\vec{e}_z$. The light gray circle is in the $\{\vec{e}_y, \vec{e}_z\}$ plane and indicates the locus of possible boresight vectors for a given cone angle α.

Of particular interest for our analysis are the periods of nearly constant cone angle $\alpha \approx 34°$ around 06:00–06:15 UTC and 12:15–14:45 UTC (purple shaded regions, Figure 9). The former segment (purple shaded, left) is located in the uniform fields over 200 R_P upstream of Pluto. We use this interval to establish a baseline for comparison to the fluxes in the latter period from 12:15–14:45 UTC (purple shaded, right). This second interval begins 15 min after NH crossed the (modeled) bow shock and entered the induced magnetosphere (see Figure 7h). During the upstream segment with $\alpha \approx 34°$ (purple shaded, left), the spacecraft performed a "plasma roll" (McComas et al., 2016), rotating three consecutive times about the Sun-Pluto line. In panel 9(e), this roll manifests as a saw-tooth feature near 06:00–06:15 UTC as the clock angle β continuously changes throughout the rotation while the cone angle remains constant. Despite the time-varying clock angle β, the orientations of the incoming He^+ velocity vectors that could be captured by the detector remained nearly unchanged due to the boresight's small cone angle ($\alpha \approx 34°$). As a result, both the modeled and observed intensities exhibit almost constant fluxes during this plasma roll. In the segment with $\alpha \approx 34°$ upstream of Pluto's induced magnetosphere, the magnitude of the modeled flux into the L09 channel (panel 9(b)) matches that of the observations within a factor of two (panel 9(c)). This demonstrates that our model can provide a quantitatively realistic description of the He^+ fluxes near Pluto. Figure 11 shows a "zoom-in" of the modeled and observed He^+ fluxes from the first three panels of Figure 9, specifically highlighting the two regions of constant $\alpha \approx 34°$.

According to Kollmann, Hill, Allen, et al. (2019), the first signature of an interaction between the energetic He^+ ions and Pluto's induced magnetosphere is visible as the "spike" just before 12:00 UTC (blue and green data points in panel 9(c)). The modeled intensities exhibit a similar spike at the same time (panels 9(a) and 9(b)). The period of constant $\alpha \approx 34°$ that occurs *downstream* of Pluto (12:15–14:45 UTC; purple shaded, right) includes NH's transition from the $y > 0$ lobe of the induced magnetotail to the $y < 0$ lobe (see Figure 7h), and ends near $x = 120\ R_P$ after the spacecraft has exited the AIKEF domain. At the start of this interval, the observed He^+ intensity for the L09 channel is depleted by a factor of 10 relative to the baseline defined for the *same* value of α in the upstream region (panel 9(c)).

In contrast to the observations, only at the lowest energies $E_{f,\mathrm{NH}}$ are the *modeled* intensities during this period noticeably reduced relative to their respective baselines (left vs. right purple segment in panel 9(a)). The magnitude of the modeled reductions diminishes when moving from lower energies up to $E_{f,\mathrm{NH}} = 88.3$ keV. Overall, the decrease in the modeled intensities is by a factor of 1.5 at most, much less than the factor of 10 that was observed by sector S0 (panel 9(c)). Considering the error bars shown in Figure 1 of Kollmann, Hill, Allen, et al. (2019), the observed reduction in the observed fluxes may be as low as a factor of five of the upstream baseline. This would indicate a somewhat closer alignment between model output and observations. The modeled fluxes gradually return to their respective baselines out to $x \approx 120\ R_P$ downstream of Pluto. However, the observability of this process is interrupted by the boresight's change of cone angle (end of purple segment in panel 9(d), near 14:45 UTC). The modeled intensity for ion energies in the range of the L09 channel does not exhibit any notable depletion within this period relative to the baseline, since this channel is above the energies where our model reveals any reductions (panel 9(b)). While our model *does* produce flux perturbations by a factor of five for the idealized setup from Figure 7 (but only at energies below L09), this is *not* the case at any point along the NH flyby trajectory when the actual look direction is included.

Around 13:30–13:45 UTC, while the spacecraft is within Pluto's induced magnetosphere, the *modeled* He^+ fluxes within the second $\alpha \approx 34°$ segment display three consecutive oscillations during which their values change by up to a factor of 1.5 for energies $E_{f,\mathrm{NH}} \leq 11.2$ keV (Figures 9a and 11a). At larger values of $E_{f,\mathrm{NH}}$, these periodic perturbations in flux gradually disappear. Within the range of the modeled channel L09 (Figures 9b and 11b), the oscillations represent changes by 30%. This periodicity in intensity coincides with another plasma roll performed by the spacecraft, as visible in the clock angle β (panel 9(e)). In contrast to the roll that occurred far upstream in *uniform* fields (06:00–06:15 UTC), there is a discernible effect of the changing clock angle on the modeled values of $\mathcal{I}$. The intensities are maximized when $\vec{L}$ has a northward component ($\beta \approx 0°$), and minimized for a

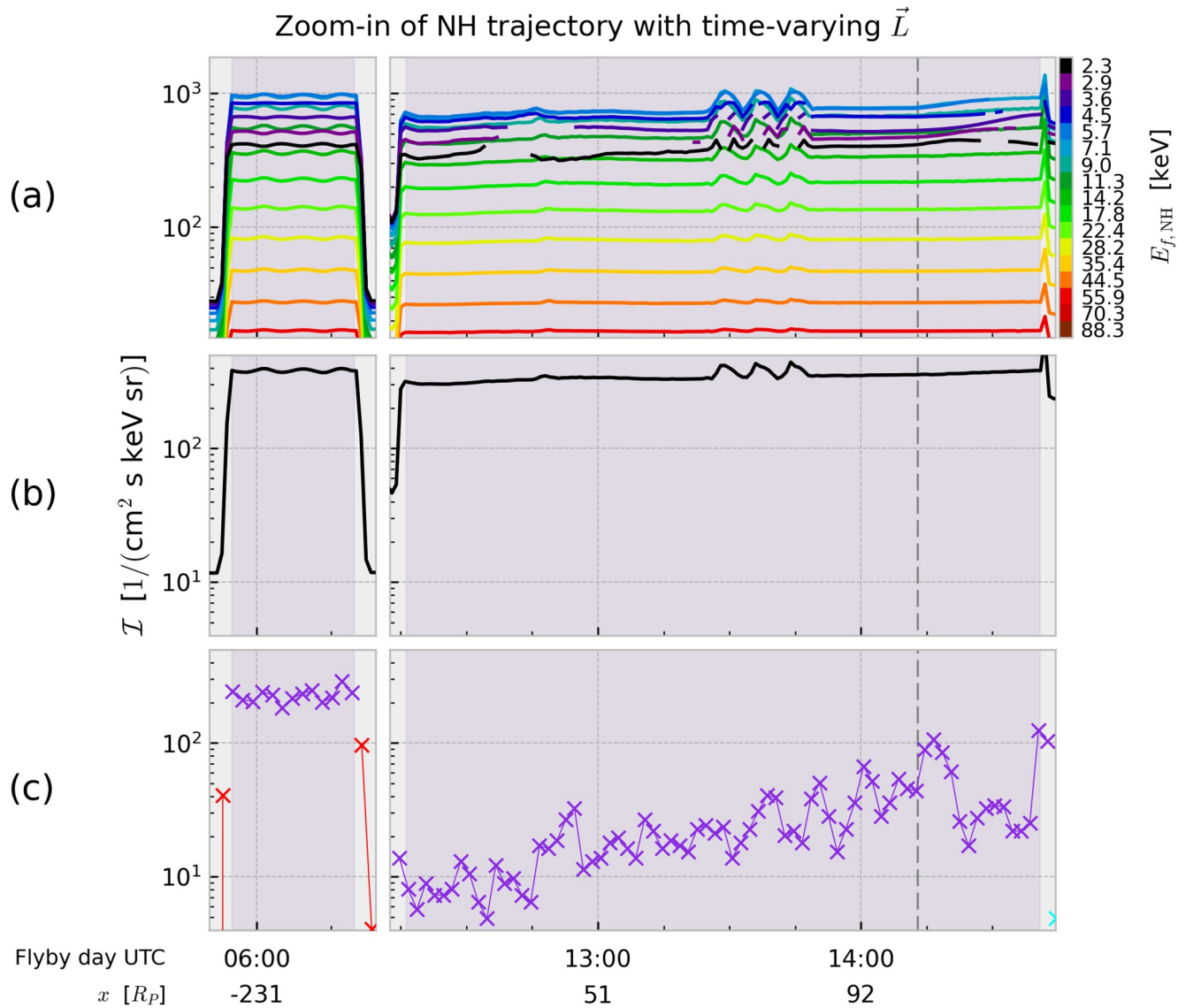

Figure 11. Zoom-in of the two purple-shaded periods with $\alpha \approx 34°$ from Figure 9. This illustration provides a closer look at the modeled (panels (a) and (b)) and observed (panel (c)) He^+ flux during these two time intervals. The vertical axis limits differ between panel (a) and panels (b) and (c). However, this axis is scaled identically in all panels, such that the magnitude of features across different panels can still be compared. The meaning of the different colors and the vertical dashed line are the same as in Figure 9.

southward component ($\beta \approx \pm 180°$). Due to the detector's small cone angle during this period ($\alpha \approx 34°$), ions need a large velocity component toward downstream to be captured. When such ions encounter the elevated magnetic field within Pluto's interaction region, the local decrease in gyroradius tends to deflect their trajectories toward the south (see also Figures 7(e) and 7(f), and Ruch et al., 2025). Hence, a boresight with a northward component ($|\beta| < 90°$) is more "favorable" for capturing these deflected ions than one with a southward component ($|\beta| > 90°$). As a result, the changing clock angle locally produces a periodicity in the modeled intensities as the detector's boresight $\vec{L}$ rotates between "favorable" and "unfavorable" look directions. Thus, only because the ions travel through non-uniform fields to reach the detector is the signature from the plasma roll visible in the intensities. The effect of the changing clock angle on the fluxes becomes weaker with increasing $E_{f,\mathrm{NH}}$, since the higher energy ions are not as strongly deflected within the induced magnetosphere (see also Ruch et al., 2025).

There is no *observed* effect of the changing clock angle on the He^+ intensities during the plasma roll near 13:30–13:45 UTC (Figure 9(c) and Kollmann, Hill, Allen, et al., 2019). Throughout the entire period between 12:30–14:30 UTC (purple shaded, right), the observed intensity is superimposed by oscillations as it gradually returns toward the baseline value (see Figure 11(c) or Figure 2 of Kollmann, Hill, Allen, et al., 2019). These periodic perturbations were suggested to stem from the ions' response to, for example, bi-ion waves that may populate Pluto's wake and can be triggered by the relative motion between the solar wind and Plutogenic pickup ions (Kollmann, Hill, Allen, et al., 2019). The *modeled* intensities for the L09 energy range (panel 9(b)) show that the signature from the plasma roll may be weaker than the amplitude of the observed oscillations. Thus, the possible effect of plasma waves in this region on energetic ion dynamics may have concealed the signature of the plasma roll in the observed He^+ intensities.

Our model traces the energetic He^+ ions through a single, static "snapshot" of the electromagnetic fields from AIKEF. Hence, the synthetic time series do not capture the effects of time-dependent phenomena (e.g., plasma waves) on energetic He^+ dynamics. For our backtracing model to accommodate any time-variabilities in the electromagnetic fields near Pluto, we would need the output from AIKEF at *multiple* points in time. Our tracing tool would then need to sample a different field cube at every timestep to emulate the passage of time. However, the required computational effort would be enormous. Since Pluto's magnetic pileup region is not able to strongly deflect the He^+ ions, we hypothesize that any bi-ion waves cannot do this either. Investigating this would still constitute a separate study. Nevertheless, using the field output from AIKEF at a single point in time allows us to, for example, isolate the clock angle dependence of $\mathcal{I}$ during the downstream plasma roll without being obscured by the influence of plasma waves or other time-dependent phenomena.

In addition to the AIKEF output from Ruch et al. (2025), we have carried out four more runs of the hybrid model. In the first two runs, the IMF orientation differs from the $\vec{B}_0 \propto -\vec{e}_y$ case. The first scenario rotates the IMF by 30° about the $+\vec{e}_x$ direction: $\vec{B}_0 = |\vec{B}_0|(0, -\cos 30°, -\sin 30°)$. This is the largest deviation from $\vec{B}_0 \propto -\vec{e}_y$ that is still within the range of possible field orientations from Zirnstein et al. (2016). The second scenario reverses the IMF direction from our original setup: $\vec{B}_0 = |\vec{B}_0|(0, +1, 0)$. Feyerabend et al. (2017) have shown that this case can still reproduce the velocity profile of the solar wind observed by SWAP near the bow shock. This scenario allows us to investigate the influence of the direction of $\vec{B}_0$ on the He^+ flux observable by PEPSSI. The modeled He^+ fluxes from these two cases are displayed in Appendix B. The synthetic time series still do not display a decrease in He^+ flux by an order of magnitude downstream of Pluto. In the third additional AIKEF run, the magnitude of the IMF is reduced to $|\vec{B}_0| = 0.10$ nT while keeping its original orientation: $\vec{B}_0 \propto -\vec{e}_y$. This IMF strength is at the lower end of the range of plausible values determined by Bagenal et al. (2015) for the NH flyby, and it is consistent with the modeling results of Barnes et al. (2019). The smaller IMF strength leads the energetic He^+ ions to possess even larger gyroradii (by a factor of $\frac{0.24\ \text{nT}}{0.10\ \text{nT}} = 2.4$), such that they are less susceptible to deflection by the non-uniform fields in the dwarf planet's interaction region. Consequently, the perturbations to their fluxes become nearly indiscernible from their respective baselines. The fourth run increases the IMF magnitude to $|\vec{B}_0| = 0.3$ nT—i.e., the highest value proposed by Bagenal et al. (2015)—while preserving the orientation along $-\vec{e}_y$. This IMF does not produce substantially stronger flux perturbations than our original setup using $\vec{B}_0 = -0.24$ nT $\vec{e}_y$. Hence, the results from the particle tracing tool for the third and fourth configurations are not shown. Overall, the output of these additional runs suggests that the discrepancy between modeled and observed time series is a robust result.

4. Summary and Concluding Remarks

The flux of heliospheric He^+ ions with energies from 2 to 100 keV, as measured by the PEPSSI instrument aboard the NH spacecraft, exhibited an unexpectedly strong, order of magnitude reduction within Pluto's induced magnetosphere (Kollmann, Hill, Allen, et al., 2019). This was despite the fact that these energetic ions travel several hundred Pluto radii over a single gyration. To provide context for these observations, we have modeled the detectability of energetic heliospheric He^+ ions by the PEPSSI instrument along the NH flyby trajectory. In addition, we have considered several hypothetical spacecraft trajectories through the induced magnetosphere (e.g., perpendicular to the Sun-Pluto line), combined with a set of idealized detector look directions. Our goal was to understand how the deflection of energetic He^+ ions by the draped electromagnetic fields near Pluto maps into PEPSSI observations. To accomplish this, we have developed a particle tracing tool that launches He^+ ions across PEPSSI's detectable energy range at the instrument's instantaneous location and propagates them backward in

time through the induced magnetosphere toward far upstream. The three-dimensional structure of the draped electromagnetic fields near Pluto is obtained using the AIKEF hybrid model (Ruch et al., 2025). The energy spectrum measured by PEPSSI upstream of Pluto (Kollmann, Hill, Allen, et al., 2019) is sampled to assign each modeled ion an intensity, allowing us to determine the He^+ flux into the detector. This process is conducted at a large number of equidistant points along the spacecraft's trajectory to generate synthetic, energy-resolved time series of He^+ flux that can be compared directly to PEPSSI observations.

Our major results are as follows:

1. The detectability of depletions in energetic He^+ flux within Pluto's induced magnetosphere heavily depends on the instrument's look direction. At a given point along the spacecraft's trajectory, different detector orientations may reveal, for example, a reduction in flux in one direction or an enhancement in flux in another. The NH spacecraft performed three consecutive rotations about the Sun-Pluto line while it was within the induced magnetosphere (referred to as the "plasma roll"). Our model results for this event demonstrate the dependence of the He^+ flux on detector look direction, showing changes by up to 30% while spinning. Hence, observed reductions in energetic He^+ flux may only partially be a consequence of the ions being excluded from the induced magnetosphere following their interaction with the perturbed fields. Instead, a crucial factor shaping these observations is the finite FOV of the PEPSSI detector, which only accepts ions with a narrow range of velocity vectors at a given time.
2. The magnitude of the modeled perturbations to He^+ flux depends on the ions' energy. Our model reveals appreciable reductions in flux only for ions near 10 keV or below, while above 20 keV the fluxes remain approximately at the unperturbed upstream values. This is consistent with the behavior of energetic ions at other small bodies, for example, Europa or Callisto, where the influence of electromagnetic perturbations on their dynamics decreases with energy (e.g., Addison et al., 2021; Liuzzo et al., 2019a).
3. The IMF near Pluto at the time of the NH flyby was not measured. Instead, it has been constrained indirectly through modeling efforts: Zirnstein et al. (2016) determined a range of IMF vectors that can explain the observations of Plutogenic pickup ions by the SWAP instrument. Additionally, Feyerabend et al. (2017) identified multiple IMF orientations that can reproduce the slowing of the solar wind at Pluto's bow shock as observed by SWAP. Hence, we calculated the energetic He^+ flux observable along the NH trajectory for several IMF orientations. The greatest reduction in modeled He^+ flux across the various IMF setups is by 50%—much less than the order of magnitude depletion that was observed—and occurred only for ion energies below 10 keV.

Overall, our particle tracing model can produce perturbations to the He^+ flux by up to a factor of five, which is comparable in magnitude to the signatures seen by NH. However, such non-uniformities in flux are only seen for idealized spacecraft trajectories and/or detector orientations, but not for the geometry of the actual NH flyby. In general, our model reveals persistently weaker (and energy-dependent) perturbations to energetic He^+ flux compared to what was observed. The discrepancy between model results and observations may partially stem from any differences in the upstream conditions used in AIKEF and their actual values during the NH flyby. This particularly holds for the IMF, which was not measured by NH. The structure of the induced magnetosphere relative to the NH flyby geometry will change with the IMF configuration used in the hybrid model, which influences the energetic ion environment. Although we sampled multiple IMF configurations, the vastness of parameter space is intractable given the computing times of a hybrid model. Additional deviations could stem from any time-dependent phenomena that are not present in our particle tracing tool, such as plasma waves. Despite its infeasibility in the near future, furthering our understanding of Pluto's induced magnetosphere and its influence on energetic heliospheric ions would be significantly bolstered by additional flybys of the system.

Appendix A: Transformation of $I_{i,\mathrm{NH}}(E_{i,\mathrm{NH}})$ into the Solar Wind Frame

To avoid ambiguities associated with the He^+ particles' gyrophase, we need to transform the observed $I_{i,\mathrm{NH}}(E_{i,\mathrm{NH}})$ spectrum into the rest frame of the solar wind, Σ_{SW}. Although the process of transforming the energy spectrum from Σ_{NH} to Σ_{SW} is independent of the backtracing procedure, we continue to use the subscript "i" in this discussion to emphasize that the spectrum in either frame corresponds to the region upstream of Pluto where the electromagnetic fields are uniform. The transformed spectrum $I_{i,\mathrm{SW}}(E_{i,\mathrm{NH}})$ is sampled in the backtracing procedure given an ion macroparticle's "initial" energy $E_{i,\mathrm{SW}}$ when it reaches the escape plane at $x = -762\ R_P$ to assign it an intensity.

The spectrum data in Σ_{NH} were collected when the boresight $\vec{L}$ of sector S0 formed a (cone) angle $\alpha \approx 34°$ against the Pluto-Sun line (see also Figure 10). For all 17 discrete energies $E_{i,NH}$ comprising the *observed* $I_{i,NH}(E_{i,NH})$ spectrum upstream (orange curve in Figure 3), we consider a set of He^+ ion macroparticles, each of them entering the instrument through a unique surface element A^λ of the discretized FOV (see also Section 2.4.2). Similar to Section 2.2, a total of $N = 300$ surface elements and individual ions are taken into account at every energy $E_{i,NH}$. Each ion's velocity vector is antiparallel to the local radial unit vector $\vec{l}$ that is normal to A^λ. Analogous to Equation 8, every ion is assigned an intensity of $\frac{1}{N} I_{i,NH}(E_{i,NH})$, with $I_{i,NH}(E_{i,NH})$ taken from the orange curve in Figure 3.

Using the Galilean transformation, each ion's velocity vector is transformed from Σ_{NH} into Σ_{SW}, yielding its energy $E_{i,SW}$. The intensity represented by the ion macroparticle in Σ_{SW} then follows from Equation 4. Subsequently, the $I_{i,SW}(E_{i,SW})$ spectrum (blue curve) is assembled by binning the individual macroparticles' contributions according to their energy $E_{i,SW}$. The spectrum in Σ_{NH} from Kollmann, Hill, Allen, et al. (2019) spans the energy range from 2 to 100 keV (orange curve in Figure 3). However, when applying the Galilean transformation to move to the Σ_{SW} frame, some ions may attain energies below this range, as low as 400 eV. Hence, additional energy bins have been included below the smallest value covered by the data from Kollmann, Hill, Allen, et al. (2019) to account for these ions. The He^+ energy spectrum in Σ_{SW} is treated as isotropic, consistent with observations (Kollmann, Hill, McNutt, et al., 2019).

Since the spacecraft was rotating about the Pluto-Sun line during the data acquisition period, this procedure was carried out at a cone angle of $\alpha = 34°$ and multiple discrete clock angles β. The $I_{i,SW}(E_{i,SW})$ spectrum (blue curve in Figure 3) was then obtained through averaging the results for the different values of β. However, we emphasize that the spectra calculated for different clock angles β are nearly identical.

For certain detector positions and FOV orientations, a backtraced ion—launched from node $\vec{r}_f$ at energy $E_{f,NH}$—may reach an upstream energy $E_{i,SW}$ *below* the smallest value covered by the $I_{i,SW}(E_{i,SW})$ curve in Figure 3 (near $E_{i,SW} \approx 400$ eV). In such a case, no modeled fluxes are shown at position $\vec{r}_f$ for this specific energy $E_{f,NH}$ (see Section 3): observations from the Pluto flyby do not allow for reconstruction of the energy spectrum below $E_{i,SW} \approx 400$ eV. However, such gaps in our model output typically affect only the lowest few detector energies $E_{f,NH}$, and this happens only for select viewing directions. Hence, omitting these points in the discussion does not have an impact on the conclusions of our study.

Appendix B: Results for the NH Flyby With Different IMF Orientations

For the NH trajectory and time-varying look direction, Figure B1 compares the modeled and observed time series of energetic He^+ intensity for an IMF vector of $\vec{B}_0 = |\vec{B}_0|(0, -\cos 30°, -\sin 30°)$. The modeled time series (panels B1(a) and B1(b)) are qualitatively very similar to those from the $\vec{B}_0 \propto -\vec{e}_y$ case (Figure 9). In other words, the modeled intensity for channel L09 (panel B1(b)) again shows minimal perturbations during the downstream interval with $\alpha \approx 34°$. The modified IMF does not produce a depletion in intensity by an order of magnitude as was observed.

Figure B2 shows the modeled time series for the scenario with a flipped IMF orientation: $\vec{B}_0 = |\vec{B}_0|(0, +1, 0)$. At the beginning of the downstream interval with $\alpha \approx 34°$ (purple shaded, right), the modeled He^+ intensities at the lowest energies ($E_{f,NH} \leq 11.3$ keV) are slightly *enhanced* by 30% relative to the respective baselines (defined by the upstream period with $\alpha \approx 34°$). The modeled intensities at higher energies—including the L09 channel (panel B2(b)))—again show minimal perturbations. Since the IMF orientation is reversed compared to the $\vec{B}_0 \propto -\vec{e}_y$ case from Figure 9, the He^+ ions gyrate in the opposite direction. Therefore, when ions with an instantaneous velocity toward downstream encounter the regions of elevated magnetic field inside the induced magnetosphere, they are deflected *northward* instead of southward. Excluding the plasma roll around 13:30 UTC, the detector's boresight $\vec{L}$ in the downstream segment with $\alpha \approx 34°$ has a southward component ($\beta \approx 180°$, see panel B2(e)). Hence, its look direction is more favorable to capture ions deflected northward. In other words, our model results imply that the reversed IMF orientation is not conducive for the detection of substantial reductions in He^+ intensity given the viewing geometry during the NH flyby.

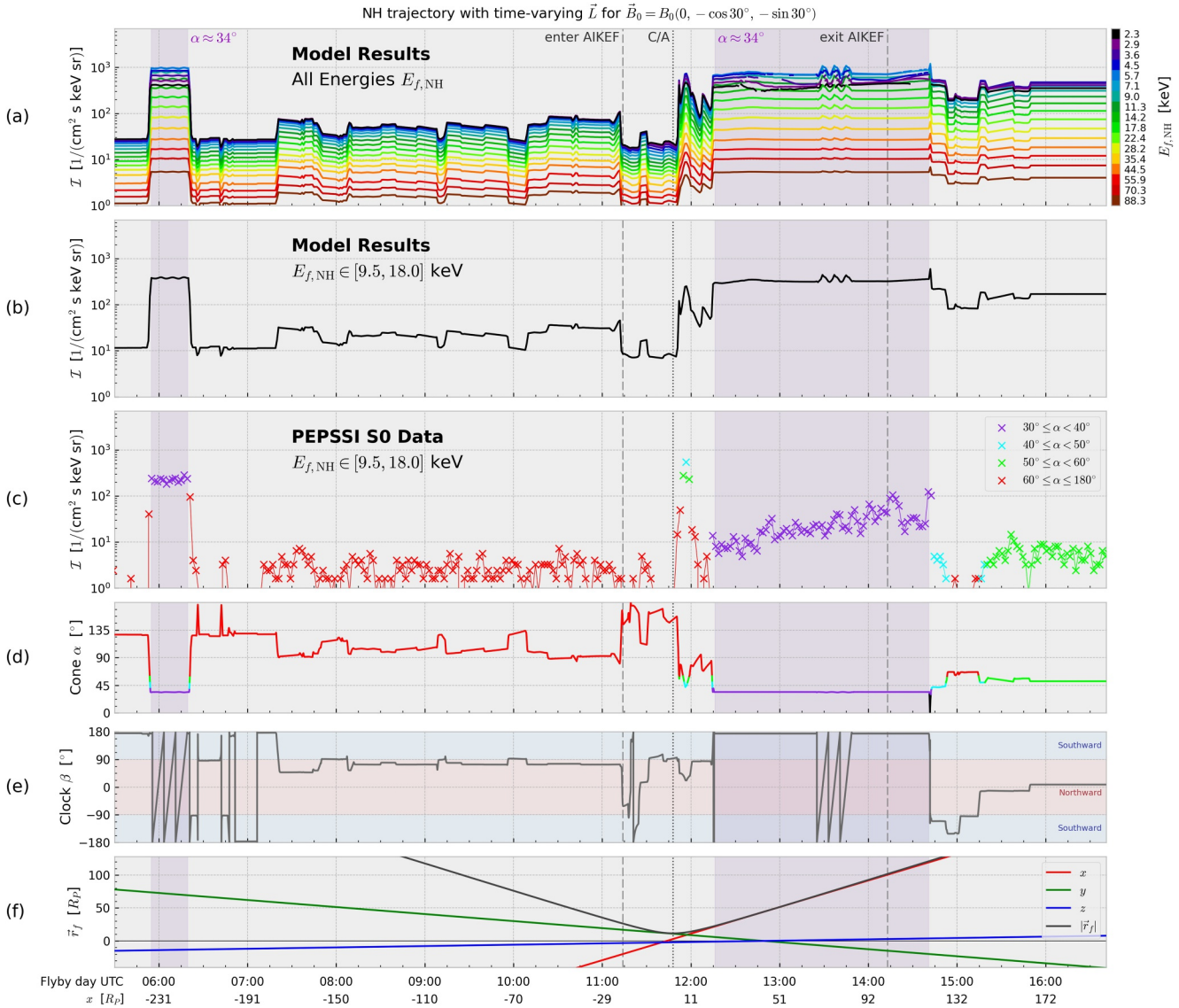

Figure B1. Modeled and observed energetic He^+ intensities along the New Horizons trajectory for an interplanetary magnetic field vector of $\vec{B}_0 = |\vec{B}_0|(0, -\cos 30°, -\sin 30°)$. The layout of the panels (a)–(f) and the quantities shown are the same as in Figure 9.

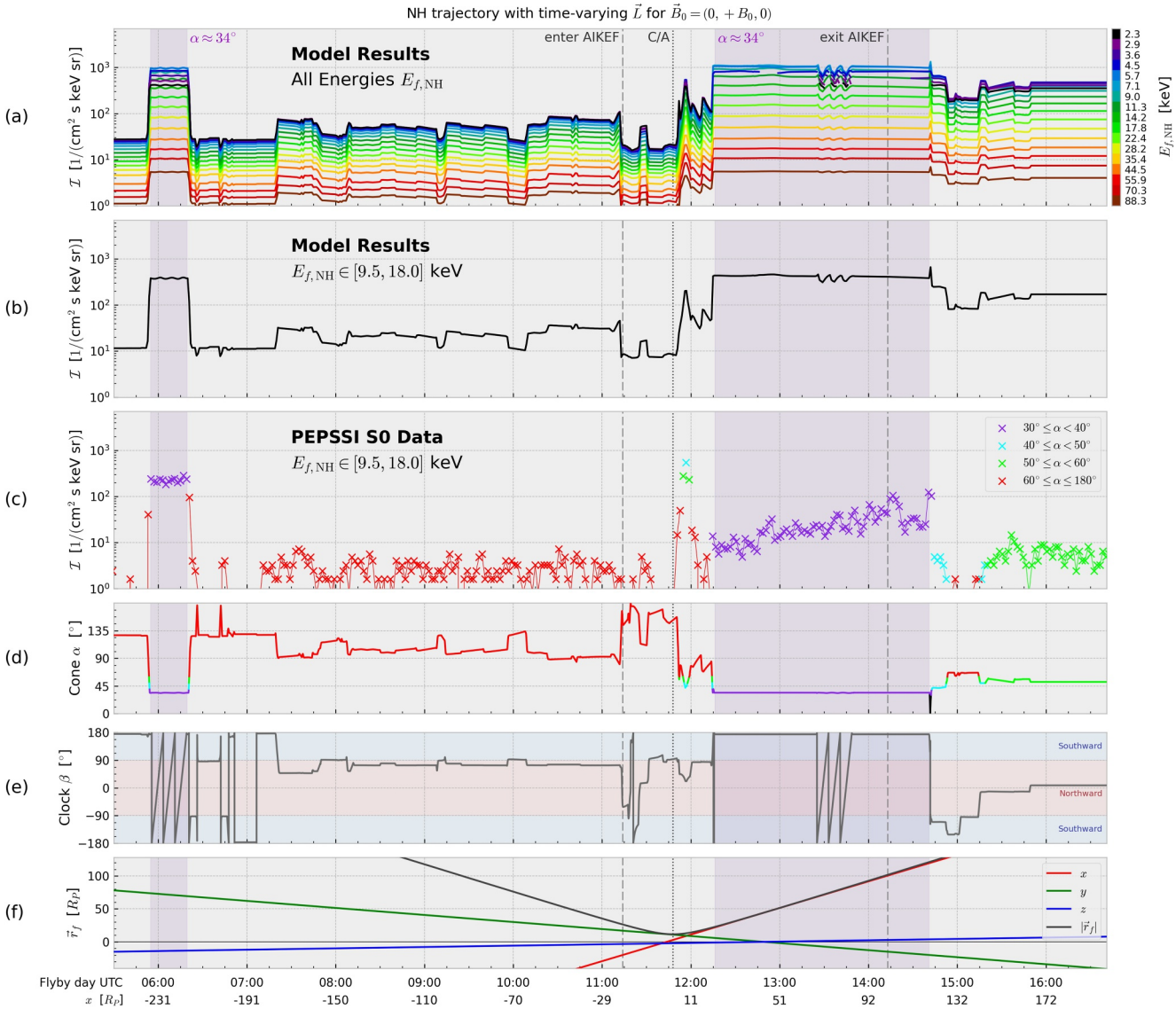

Figure B2. Modeled and observed energetic ion intensities along the New Horizons trajectory for an interplanetary magnetic field vector of $\vec{B}_0 = |\vec{B}_0|(0, +1, 0)$. The layout of the Figure is the same as that of Figure B1.

Conflict of Interest

The authors declare no conflicts of interest relevant to this study.

Acknowledgments

The authors acknowledge financial support through NASA's *Solar System Workings Program* 2021, Grant 80NSSC23K0352. The computing resources used to carry out the AIKEF and particle tracing runs were provided by the NASA High-End Computing program through the NASA Advanced Supercomputing division at Ames Research Center. This body of work was not written nor contributed to in any part by an artificial intelligence engine. The authors would like to thank both referees for careful inspection of the manuscript and for valuable comments.

Availability Statement

Data supporting the production and conclusions of this work can be obtained from Ruch et al. (2026). The mission-specific SPICE kernels containing the relevant ephemerides for NH can be found on the Planetary Data System (Steffl et al., 2010).

References

Acton, C. (1996). Ancillary data services of NASA's navigation and ancillary information facility. *Planetary and Space Science*, *44*(1), 65–70. https://doi.org/10.1016/0032-0633(95)00107-7

Acton, C., Bachman, N., Semenov, B., & Wright, E. (2018). A look towards the future in the handling of space science mission geometry. *Planetary and Space Science*, *150*, 9–12. https://doi.org/10.1016/j.pss.2017.02.013

Addison, P., Haynes, C. M., Stahl, A. M., Liuzzo, L., & Simon, S. (2024). Magnetic signatures of the interaction between Europa and Jupiter's magnetosphere during the Juno flyby. *Geophysical Research Letters*, *51*(2), e2023GL106810. https://doi.org/10.1029/2023GL106810

Addison, P., Liuzzo, L., Arnold, H., & Simon, S. (2021). Influence of Europa's time-varying electromagnetic environment on magnetospheric ion precipitation and surface weathering. *Journal of Geophysical Research: Space Physics*, *126*(5), e2020JA029087. https://doi.org/10.1029/2020JA029087

Addison, P., Liuzzo, L., & Simon, S. (2022). Effect of the magnetospheric plasma interaction and solar illumination on ion sputtering of Europa's surface ice. *Journal of Geophysical Research: Space Physics*, *127*(2), e2021JA030136. https://doi.org/10.1029/2021JA030136

Addison, P., Liuzzo, L., & Simon, S. (2023). Surface-plasma interactions at Europa in draped magnetospheric fields: The contribution of energetic electrons to energy deposition and sputtering. *Journal of Geophysical Research: Space Physics*, *128*(8), e2023JA031734. https://doi.org/10.1029/2023JA031734

Bagenal, F., Delamere, P. A., Elliott, H. A., Hill, M. E., Lisse, C. M., McComas, D. J., et al. (2015). Solar wind at 33 AU: Setting bounds on the Pluto interaction for new Horizons. *Journal of Geophysical Research (Planets)*, *120*(9), 1497–1511. https://doi.org/10.1002/2015JE004880

Bagenal, F., Horányi, M., McComas, D. J., McNutt, R. L., Elliott, H. A., Hill, M. E., et al. (2016). Pluto' interaction with its space environment: Solar wind, energetic particles, and dust. *Science*, *351*(6279), aad9045. https://doi.org/10.1126/science.aad9045

Barnes, N. P. (2024). *Obstacles to plasma flow in an ion kinetic regime: Application to a terrestrial ionospheric active plasma experiment and new Horizons observations of the Pluto system*. (Doctoral dissertation, University of Alaska Fairbanks). Retrieved from http://hdl.handle.net/11122/15129

Barnes, N. P., Delamere, P. A., Strobel, D. F., Bagenal, F., McComas, D. J., Elliott, H. A., et al. (2019). Constraining the IMF at Pluto using new Horizons SWAP data and hybrid simulations. *Journal of Geophysical Research (Space Physics)*, *124*(3), 1568–1581. https://doi.org/10.1029/2018JA026083

Bell, A. R. (1978). The acceleration of cosmic rays in shock fronts – I. *Monthly Notices of the Royal Astronomical Society*, *182*(2), 147–156. https://doi.org/10.1093/mnras/182.2.147

Cheng, A. F., Weaver, H. A., Conard, S. J., Morgan, M. F., Barnouin-Jha, O., Boldt, J. D., et al. (2008). Long-range reconnaissance imager on new Horizons. *Space Science Reviews*, *140*(1–4), 189–215. https://doi.org/10.1007/s11214-007-9271-6

Delamere, P. A. (2009). Hybrid code simulations of the solar wind interaction with Pluto. *Journal of Geophysical Research (Space Physics)*, *114*(A3), A03220. https://doi.org/10.1029/2008JA013756

Feyerabend, M., Liuzzo, L., Simon, S., & Motschmann, U. (2017). A three-dimensional model of Pluto's interaction with the solar wind during the new Horizons encounter. *Journal of Geophysical Research: Space Physics*, *122*(10), 10356–10368. https://doi.org/10.1002/2017JA024456

Fisk, L. A., & Gloeckler, G. (2007). Thermodynamic constraints on stochastic acceleration in compressional turbulence. *Proceedings of the National Academy of Sciences*, *104*(14), 5749–5754. https://doi.org/10.1073/pnas.0700881104

Fisk, L. A., & Gloeckler, G. (2014). The case for a common spectrum of particles accelerated in the heliosphere: Observations and theory. *Journal of Geophysical Research: Space Physics*, *119*(11), 8733–8749. https://doi.org/10.1002/2014JA020426

Gladstone, G. R., Stern, S. A., Ennico, K., Olkin, C. B., Weaver, H. A., Young, L. A., et al. (2016). The atmosphere of Pluto as observed by new Horizons. *Science*, *351*(6279), aad8866. https://doi.org/10.1126/science.aad8866

Haynes, C. M., Simon, S., & Liuzzo, L. (2025a). Emission of energetic neutral atoms from Ganymede's magnetosphere-atmosphere interaction. *Journal of Geophysical Research: Space Physics*, *130*(10), e2025JA034469. https://doi.org/10.1029/2025JA034469

Haynes, C. M., Tippens, T., Addison, P., Liuzzo, L., Poppe, A. R., & Simon, S. (2023). Emission of energetic neutral atoms from the magnetosphere-atmosphere interactions at callisto and Europa. *Journal of Geophysical Research: Space Physics*, *128*(10), e2023JA031931. https://doi.org/10.1029/2023JA031931

Haynes, C. M., Tippens, T., Simon, S., & Liuzzo, L. (2025b). Constraints on the observability of energetic neutral atoms from the magnetosphere-atmosphere interactions at callisto and Europa. *Journal of Geophysical Research: Space Physics*, *130*(1), e2024JA033391. https://doi.org/10.1029/2024JA033391

Hinson, D., Linscott, I., Strobel, D., Tyler, G., Bird, M., Pätzold, M., et al. (2018). An upper limit on Pluto's ionosphere from radio occultation measurements with new Horizons. *Icarus*, *307*, 17–24. https://doi.org/10.1016/j.icarus.2018.02.011

Kollmann, P., Hill, M. E., Allen, R. C., McNuttJr., R. L., Brown, L. E., Barnes, N. P., et al. (2019a). Pluto's interaction with energetic heliospheric ions. *Journal of Geophysical Research: Space Physics*, *124*(9), 7413–7424. https://doi.org/10.1029/2019JA026830

Kollmann, P., Hill, M. E., McNutt, R. L., Brown, L. E., Allen, R. C., Clark, G., et al. (2019b). Suprathermal ions in the outer heliosphere. *The Astrophysical Journal*, *876*(1), 46. https://doi.org/10.3847/1538-4357/ab125f

Krasnopolsky, V. A. (2020). A photochemical model of Pluto's atmosphere and ionosphere. *Icarus*, *335*, 113374. https://doi.org/10.1016/j.icarus.2019.07.008

Liuzzo, L., Feyerabend, M., Simon, S., & Motschmann, U. (2015). The impact of Callisto's atmosphere on its plasma interaction with the Jovian magnetosphere. *Journal of Geophysical Research (Space Physics)*, *120*(11), 9401–9427. https://doi.org/10.1002/2015JA021792

Liuzzo, L., Poppe, A. R., Nénon, Q., Simon, S., & Addison, P. (2024). Constraining the influence of Callisto's perturbed electromagnetic environment on energetic particle observations. *Journal of Geophysical Research: Space Physics*, *129*(2), e2023JA032189. https://doi.org/10.1029/2023ja032189

Liuzzo, L., Simon, S., Feyerabend, M., & Motschmann, U. (2016). Disentangling plasma interaction and induction signatures at callisto: The galileo C10 flyby. *Journal of Geophysical Research: Space Physics*, *121*(9), 8677–8694. https://doi.org/10.1002/2016JA023236

Liuzzo, L., Simon, S., Feyerabend, M., & Motschmann, U. (2017). Magnetic signatures of plasma interaction and induction at callisto: The galileo C21, C22, C23, and C30 flybys. *Journal of Geophysical Research: Space Physics*, *122*(7), 7364–7386. https://doi.org/10.1002/2017JA024303

Liuzzo, L., Simon, S., & Regoli, L. (2019a). Energetic electron dynamics near callisto. *Planetary and Space Science*, *179*, 104726. https://doi.org/10.1016/j.pss.2019.104726

Liuzzo, L., Simon, S., & Regoli, L. (2019b). Energetic ion dynamics near callisto. *Planetary and Space Science*, *166*, 23–53. https://doi.org/10.1016/j.pss.2018.07.014

McComas, D. J., Allegrini, F., Bagenal, F., Casey, P., Delamere, P., Demkee, D., et al. (2007). The solar wind around pluto (SWAP) instrument aboard new Horizons. *Space Science Reviews*, *140*(1–4), 261–313. https://doi.org/10.1007/s11214-007-9205-3

McComas, D. J., Elliott, H. A., Weidner, S., Valek, P., Zirnstein, E. J., Bagenal, F., et al. (2016). Pluto's interaction with the solar wind. *Journal of Geophysical Research (Space Physics)*, *121*(5), 4232–4246. https://doi.org/10.1002/2016JA022599

McNutt, R. L., Livi, S. A., Gurnee, R. S., Hill, M. E., Cooper, K. A., Andrews, G. B., et al. (2008). The pluto energetic particle spectrometer science investigation (PEPSSI) on the new Horizons mission. *Space Science Reviews*, *140*(1–4), 315–385. https://doi.org/10.1007/s11214-008-9436-y

Müller, J., Simon, S., Motschmann, U., Schüle, J., Glassmeier, K., & Pringle, G. J. (2011). A.I.K.E.F.: Adaptive hybrid model for space plasma simulations. *Computer Physics Communications*, *182*(4), 946–966. https://doi.org/10.1016/j.cpc.2010.12.033

Nordheim, T. A., Regoli, L. H., Harris, C. D. K., Paranicas, C., Hand, K. P., & Jia, X. (2022). Magnetospheric ion bombardment of europa's surface. *The Planetary Science Journal*, *3*(1), 5. https://doi.org/10.3847/PSJ/ac382a

Ruch, R. T., Simon, S., & Haynes, C. M. (2025). Dynamics of energetic heliospheric ions in pluto's induced magnetosphere. *Journal of Geophysical Research: Space Physics*, *130*(2), e2024JA033548. https://doi.org/10.1029/2024JA033548

Ruch, R. T., Simon, S., Haynes, C. M., & Kollmann, P. (2026). Data for "Modeling the Detectability of Energetic Heliospheric Ions at Pluto During the New Horizons Flyby" by Ruch et al., 2026 [Dataset]. *Zenodo*. https://doi.org/10.5281/zenodo.18702057

Simon, S., Boesswetter, A., Bagdonat, T., Motschmann, U., & Glassmeier, K.-H. (2006). Plasma environment of Titan: A 3-d hybrid simulation study. *Annals of Geophysics*, *24*(3), 1113–1135. https://doi.org/10.5194/angeo-24-1113-2006

Stahl, A., Addison, P., Simon, S., & Liuzzo, L. (2023). A model of Ganymede's magnetic and plasma environment during the juno PJ34 flyby. *Journal of Geophysical Research: Space Physics*, *128*(12), e2023JA032113. https://doi.org/10.1029/2023ja032113

Steffl, A. J., Peterson, J., Carcich, B., Nguyen, L., & Stern, S. A. (2010). *New Horizons spice kernels V1.0*. NASA Planetary Data System. id. NH-J/P/SS-SPICE-6-V1.0. https://doi.org/10.17189/1520109

Stern, S. A., Kammer, J., Gladstone, G., Steffl, A., Cheng, A., Young, L., et al. (2017). New Horizons constraints on Charon's present day atmosphere. *Icarus*, *287*, 124–130. https://doi.org/10.1016/j.icarus.2016.09.019

Stern, S. A., Slater, D. C., Scherrer, J., Stone, J., Dirks, G., Versteeg, M., et al. (2008). ALICE: The ultraviolet imaging spectrograph aboard the new Horizons pluto–kuiper belt mission. *Space Science Reviews*, *140*(1–4), 155–187. https://doi.org/10.1007/s11214-008-9407-3

Tippens, T., Liuzzo, L., & Simon, S. (2022). Influence of Titan's variable electromagnetic environment on the global distribution of energetic neutral atoms. *Journal of Geophysical Research: Space Physics*, *127*(10), e2022JA030722. https://doi.org/10.1029/2022ja030722

Tippens, T., Roussos, E., Simon, S., & Liuzzo, L. (2024a). A novel backtracing model to study the emission of energetic neutral atoms at Titan. *Journal of Geophysical Research: Space Physics*, *129*(1), e2023JA032083. https://doi.org/10.1029/2023ja032083

Tippens, T., Simon, S., & Roussos, E. (2024b). Modeling the emission of energetic neutral atoms in titan's dynamic magnetospheric environment. *Journal of Geophysical Research: Space Physics*, *129*(11), e2024JA033103. https://doi.org/10.1029/2024JA033103

Young, L. A., Kammer, J. A., Steffl, A. J., Gladstone, G. R., Summers, M. E., Strobel, D. F., et al. (2017). Structure and composition of Pluto's atmosphere from the new Horizons solar ultraviolet occultation. *Icarus*, *300*, 174–199. https://doi.org/10.1016/j.icarus.2017.09.006

Zirnstein, E. J., McComas, D. J., Elliott, H. A., Weidner, S., Valek, P. W., Bagenal, F., et al. (2016). Interplanetary magnetic field sector from solar wind around pluto (SWAP) measurements of heavy ion pickup near Pluto. *The Astrophysical Journal*, *823*(2), L30. https://doi.org/10.3847/2041-8205/823/2/L30